

NACA RM L53L24a

7516

DL44271



TECH LIBRARY KAFB, NM



# RESEARCH MEMORANDUM

EFFECT OF SOME SECTION MODIFICATIONS AND PROTUBERANCES  
ON THE ZERO-LIFT DRAG OF DELTA WINGS AT TRANSONIC  
AND SUPERSONIC SPEEDS

By Carl A. Sandahl and William E. Stoney

Langley Aeronautical Laboratory  
Langley Field, Va.

NATIONAL ADVISORY COMMITTEE  
FOR AERONAUTICS

WASHINGTON  
February 18, 1954

Classification Code: Unclassified  
By Authority of Nasa Tech Pub Announcement #123

By 7 Jan 58  
NK

GRADE OF OFFICER MAKING CHANGE  
27 Mar 61  
DATE



## NATIONAL ADVISORY COMMITTEE FOR AERONAUTICS

## RESEARCH MEMORANDUM

EFFECT OF SOME SECTION MODIFICATIONS AND PROTUBERANCES  
ON THE ZERO-LIFT DRAG OF DELTA WINGS AT TRANSONIC  
AND SUPERSONIC SPEEDS

By Carl A. Sandahl and William E. Stoney

## SUMMARY

Free-flight rocket model tests have been made at Mach numbers extending from approximately 0.8 to 1.9 to determine the effect of leading-edge radius and airfoil aftersection thickening on the zero-lift drag of a 60° delta wing. In addition, one configuration employed simulated control-actuator housings. For the subsonic leading-edge condition of the tests, increasing the leading-edge radius had no measurable effect on the drag coefficient. A small but finite thickening of the airfoil aftersection which did not increase the trailing-edge thickness resulted in a slight increase in drag coefficient. Further thickening of the aftersection resulted in substantial increases in drag coefficient. At supersonic speeds, the drag coefficient increased nearly linearly with those values of trailing-edge thickness tested. Increasing the section thickness ratio near the wing tip while maintaining straight-line constant-percent-chord wing-surface elements resulted in no measurable drag increment. Linear theory generally predicted absolute values of wing pressure drag coefficients larger than those derived from the experiments, but predicted effects of section changes accurately.

## INTRODUCTION

Thin delta wings are of considerable current interest in the design of transonic airplanes. In such designs it often appears desirable from structural and volume considerations to increase the wing section thickness fore and aft of the position of maximum thickness while maintaining the maximum thickness constant. It may also be desirable to increase the leading-edge radius in order to reduce the drag at lift. Generally, all the foregoing section changes may be expected to increase the zero-lift drag. It was the primary purpose of the investigation reported herein to assess the zero-lift drag penalties arising from such section

*Handwritten signature/initials*

modifications for a  $60^\circ$  delta wing. The basic airfoil section was of the NACA 000X-X3 family of reference 1. The leading-edge radius was varied from zero to three times that normally used with the basic section. The airfoil aftersection was varied systematically from that of the basic section to one having parallel sides extending back from the maximum-thickness position. For one test, the basic wing was equipped with rather large simulated control-actuator housings.

The Mach number range of the tests was from approximately 0.8 to 1.9. The corresponding Reynolds numbers varied from  $6.5 \times 10^6$  to  $27.4 \times 10^6$  based on the wing mean aerodynamic chord.

Free-flight rocket-propelled test vehicles were employed. The models were launched at the Langley Pilotless Aircraft Research Station at Wallops Island, Va.

#### SYMBOLS

$C_D$	configuration drag coefficient based on $S_w$
$C_{Dw}$	wing-plus-interference drag coefficient based on $S_w$
$C_{Dp}$	wing pressure drag coefficient based on $S_w$
$S_w$	wing area obtained by extending leading and trailing edges to center line (equal to 7.57 sq ft for all models except model 10 for which $S_w$ equals 4.55 sq ft)
$W$	model weight, sustainer motor fuel expended
$V$	velocity tangent to flight path or volume of wing external to fuselage
$a$	linear acceleration tangent to flight path
$g$	acceleration due to gravity
$\rho$	mass density of air
$\gamma$	flight-path angle measured from horizontal
$M$	Mach number
$R$	Reynolds number based on $\bar{c}$

$\Lambda_{LE}$	leading-edge sweep
$\Lambda_{TE}$	trailing-edge sweep
b	actual wing span
b'	wing span measured to theoretical wing tips
c	local wing chord
$c_f$	wing chord over which section sides are parallel
$\bar{c}$	wing mean aerodynamic chord
t	section maximum thickness
h	section trailing-edge thickness
A	configuration cross-sectional area
r	radius of equivalent body of revolution
x	distance from fuselage nose
l	fuselage length

#### MODELS

The general arrangement of the test configuration is shown in figures 1 and 2. The fuselage ordinates are presented in table I. A list of configurations tested is in table II.

The fuselages were constructed mainly of laminated wood. The wings had a balsa-mahogany core to which 0.020-inch-thick duralumin plates were bonded to form the outer surfaces. The wing tips and trailing edges were stiffened by means of a chord-plane insert of 0.064-inch-thick duralumin. The vertical tails were of duralumin.

The geometry of the wings used is shown in figures 3 to 6. The airfoil sections are defined in reference 1. The wing of model 11 was a 60° delta wing with an NACA 65A003 airfoil section. The notched wing of model 10, figure 5, was obtained by removing the flat region of the wing of model 6, figure 4, and shearing the airfoil aftersections forward. Both wings had the same absolute maximum thickness.

The wing of model 12 was equipped with simulated control-actuator housings as shown in figure 6. The housings were scaled from those on the top side of the wing of a current airplane. For the test, duplicate housings were employed on both sides of the wing to ensure zero-lift flight and a measurable drag increment. The drag-coefficient increment would be approximately doubled by this procedure. The housings were of maximum breadth and thickness at, and were all identical aft of, the hypothetical control hinge line which was located at 90 percent of the theoretical root chord and was parallel to the wing trailing edge. In side view, the housings are defined by parabolic arcs with vertices above and below the chord plane at the hinge line, tangent to the wing surface at the front end, and intercepting the trailing edge. In plan view, the housings are defined by similar parabolic arcs. A photograph of this model is shown in figure 7.

The longitudinal distribution of cross-sectional area for all models is shown in figures 8 to 10.

#### TEST METHOD

##### Propulsion

The models were accelerated to supersonic speeds by a two-stage rocket propulsion system. The first stage was either a 5-inch HPAG rocket motor or a 6-inch ABL Deacon rocket motor yielding maximum Mach numbers of approximately 1.5 and 1.9, respectively. In all cases the second stage (sustainer) was a 3.25-inch Mk. 7 rocket motor. A photograph of the model-booster-launcher arrangement preparatory to launching is shown in figure 11.

##### Instrumentation

The instrumentation, none of which was contained within the models, included a CW Doppler velocimeter radar, a modified SCR 584 position radar, and radiosonde equipment. The Doppler velocimeter produced a time history of the radial component of the model velocity relative to the launching site. The position radar produced a time history of model position in space. The radiosonde units, which were launched immediately after the test flights, were tracked during their ascent with the space position radar permitting the determination of the speed and direction of winds aloft in addition to the usual pressure and temperature measurements.

## Data Reduction

The drag coefficients of the models were obtained during coasting flight by evaluating the expression

$$C_D = \frac{-2W(a + g \sin \gamma)}{g\rho V^2 S_w}$$

In the evaluation, the position-radar record was reduced to a plot of altitude against horizontal range. From this flight-path plot, trigonometric corrections were obtained which were applied to the CW Doppler data to convert radial velocity to tangential velocity along the flight path. The component of the wind velocity parallel to the flight-path was then added to obtain airspeed. The acceleration along the flight path was obtained by numerical differentiation of the tangential velocity. Mach number and Reynolds number were also obtained from the radar and radiosonde data.

The errors are estimated to be within the following limits:

$C_D$ . . . . .	$\pm 0.0007$
$M$ . . . . .	$\pm 0.005$

The errors in wing-plus-interference drag coefficients obtained by subtracting fuselage drag from wing-fuselage drag may be somewhat larger. A typical set of test results is shown in figure 12 to illustrate the continuity and scatter of the data.

## RESULTS AND DISCUSSION

The variation of Reynolds number with Mach number for the tests is shown in figure 13. The results for each model are presented in figure 14 wherein are plotted the total-drag coefficients and the wing-plus-interference drag coefficients obtained by subtracting body-drag coefficients from the total-drag coefficients. The experimentally determined body-drag coefficients, based on the two values of total wing area employed in the tests, are shown in figure 15. The curve labeled "4 fins" was obtained from a free-flight test of a four-fin wingless body identical to that used with the winged models of the tests. The decrement in drag resulting from decreasing the number of fins from four to two was obtained from experimental results in reference 2 obtained with geometrically similar fins mounted on a cylindrical fuselage. The drag coefficients for the body with the two fins so obtained were subtracted from

the drag coefficients for the winged two-fin models to obtain wing-plus-interference drag coefficients. It should be noted that this subtractive process renders the wing-plus-interference drag coefficients subject to additional errors in the regions where the drag coefficients change rapidly with Mach number (as near  $M = 1.0$ ) because of the combined errors in Mach number and drag coefficient.

Effect of leading-edge radius.- The effect of leading-edge radius is shown in figure 16 to be small and within the experimental accuracy for the range of radii tested. It should be noted that the leading edge was always subsonic.

Effect of flat midsection.- The effect of flat midsections is shown in figure 17. No measurable increases in drag coefficient over that of the basic section were obtained for  $c_f/c = 0.2$ . The larger values of  $c_f/c$  resulted in substantial reductions in critical Mach number and increases in supersonic drag. For  $c_f/c = 0.7$ , the trailing-edge thickness becomes equal to the maximum section thickness. Pressures acting on this base cause the large drag increment obtained for this configuration over the entire Mach number range investigated.

In figure 18 is shown a comparison of wing pressure drag coefficients calculated by the method described in the appendix with those derived from the data for the models of figure 17. The wing pressure drag coefficients were derived from the experimental results by subtracting the wing-friction-drag coefficients from the wing-plus-interference drag coefficients at the Mach numbers noted in figure 18. The wing-friction-drag coefficients were obtained by adjusting the subsonic-wing-plus-interference drag coefficient of the basic configuration (model 3) to the appropriate Mach and Reynolds numbers using the theoretical variations of turbulent-skin-friction coefficient with Mach number and Reynolds number given in reference 3. In figure 18(a) it will be noted that the theoretical drag coefficients are generally larger than those experimentally derived. In figure 18(b) the theoretical and the derived increments in pressure drag coefficients due to the flat midsections are seen to be in good agreement. It should be noted that the theory increasingly overestimates the pressure drag coefficient as the Mach lines approach the leading edge.

In figure 19 is plotted the ratio of wing-plus-interference drag coefficient of the flat midsection wings to that of the basic section as a function of the relative wing volume. The curves were faired by giving less regard to those test points at a relative volume of 1.11 because they appear questionable on the basis of theory noted previously. The results indicate that some increases in wing volume can be obtained with small drag penalty. Further increases in volume result in large increases in drag.



Effect of trailing-edge thickness.- The effect of trailing-edge thickness is shown in figure 20 wherein are plotted the total-drag coefficients for configurations having trailing-edge thicknesses equal to 0, 30, and 100 percent of the wing maximum thickness. At supersonic speeds, the drag coefficients increase nearly linearly, within the experimental accuracy, with those values of trailing-edge thickness tested. Also shown in figure 20 are drag-coefficient curves obtained, at supersonic speeds, by adding the increments in wing drag coefficient due to trailing-edge thickness, calculated as described in the appendix, to the measured drag coefficients of model 3 ( $h/t = 0$ ). In the Mach number range from 0.8 to 1.0, the calculated values were obtained by adding the base drag coefficients, calculated from the base pressure measurements of reference 4, to the drag coefficients of model 3. Excellent agreement is shown in this comparison at supersonic speeds. At subsonic speeds, the calculated values are substantially higher than the experimental values, indicating a reduction in wing drag exclusive of that contributed by the base with increasing  $h/t$ . In figure 21 is shown a comparison of the wing pressure drag coefficients calculated by the method of the appendix with those derived from the experiments in the manner described in the discussion of figure 18. The calculated values are generally higher than those experimentally derived; the calculations do, however, indicate accurately the trends.

Effect of trailing-edge sweep.- In figure 22 is shown the effect on the wing-plus-interference drag coefficient of removing the flat region of wing of model 6 ( $c_f/c = 0.4$ ) and shearing the aftersections forward. The thickness ratio of the resulting wing varied from 0.05 at the theoretical root to 0.10 at the 90-percent semispan station. This wing was considered to be structurally feasible while offering the possibility of low drag at low supersonic speeds. The drag coefficients are based on the total wing areas of the individual models. Substantial drag reductions were indeed obtained at Mach numbers less than approximately 1.2; at higher Mach numbers, the sheared wing had higher drag. As noted previously, the abrupt changes in  $C_{D_w}$  near  $M = 1.0$  are believed to result from the subtractive process by which this quantity was obtained.

Effect of model scale.- The effect of model scale is illustrated in figure 23 wherein the results for model 11 are compared with those for a geometrically similar twice scale model (model 4, from ref. 2). The differences are within the experimental errors and, particularly for total configuration drag coefficients at supersonic speeds, are in the direction and of the magnitude calculable on the basis of changes in skin-friction coefficient.

Effect of spanwise variation of section thickness ratio.- The effect of spanwise variation in thickness ratio may be noted in figure 14 by comparing the results for model 3, in which the wing section thickness

ratio varied from 0.03 at the root to 0.06 at the 90-percent-semispan station, with those for model 11 in which the section thickness ratio was constant at 0.03. Calculations by the method of the appendix showed that no measurable differences in wing drag could be attributed to the different wing sections employed in the two models. For the range of Mach numbers for which the foregoing comparison can be made, no measurable differences in drag exist.

Effect of simulated control-actuator housings.— The effect of the control-actuator housings on the drag is shown in figure 24 wherein are compared results for the basic wing, the wing with housings, and a wing with a flat airfoil midsection with approximately the same volume as that of wing and housing. At low supersonic speeds, the increment in drag coefficient is substantial and approximately as large as that for the wing having  $c_f/c = 0.4$ . It should be noted, as pointed out in the "Models" section, that this increment is approximately twice that which would be obtained for a more realistic situation with the housings on only one side of the wing. Also shown in figure 24 is the estimated drag coefficient for model 12 obtained by adding to the drag coefficient of model 3 an increment estimated for the housings by (1) calculating the longitudinal distribution of cross-sectional area external to the basic wing produced by the upper and lower housings at each spanwise station at which housings were attached, (2) obtaining the equivalent bodies of revolution (6 in number), and (3) estimating (from ref. 5) and summing the drag of the bodies. The estimate so obtained is low at low supersonic speeds because of interference effects between the housings and improves with increasing Mach number as these interferences become smaller.

### CONCLUSIONS

The present investigation made to determine the effect of some modifications and protuberances on the zero-lift drag of delta wings at transonic and supersonic speeds indicated the following:

1. For the subsonic leading-edge condition of the tests, increasing the leading-edge radius had no effect on the drag coefficient.
2. A small but finite thickening of the airfoil aftersection which did not increase the trailing-edge thickness resulted in no measurable increases in the drag coefficient. Additional thickening of the aftersection resulted in substantial increases in drag coefficient.
3. At supersonic speeds, the drag coefficient increased nearly linearly with those values of trailing-edge thickness tested.

4. Increasing the wing section thickness ratio at the 90-percent-semispan station from 0.03 to 0.06 while maintaining straight-line constant-percent-chord wing-surface elements and a root thickness ratio of 0.03 resulted in no measurable drag increment.

5. Multislope linear-theory methods for calculating wing pressure drag coefficients combined with experimental base pressure values generally yielded absolute values which were larger than those derived from the experiments, but accurately predicted effects of section changes.

Langley Aeronautical Laboratory,  
National Advisory Committee for Aeronautics,  
Langley Field, Va., December 8, 1953.

## APPENDIX

## THEORETICAL CALCULATIONS

The theoretical calculations of the wing wave drag were made by the method of reference 6. In this method the airfoil section is approximated by a many-sided polygon and the drag coefficients are obtained by superimposing the known solutions for single triangular wings of constant slope. This is identical to the procedure followed in reference 7 in the calculation of the drag of two- and three-slope wings.

The number of sides necessary depends somewhat on the shape of the airfoil section; however, it was shown in reference 6 for a circular-arc wing that the calculated drag was essentially constant above a division into 10 slopes. One of the present airfoils was calculated using 10-sided and 20-sided figures and the results were identical for Mach numbers where the leading edge was subsonic. For cases where the Mach line lies on or behind the leading edge, the drag calculated by this method for any round-nose airfoil is incorrect since it approaches infinity as the number of sides is increased. This is due to the stagnation condition at the leading edge for which the linear theory is inapplicable. The present calculations were extended to the supersonic leading-edge cases since it is the change in drag with change in shape after the maximum thickness that is of interest and this should be reasonably independent of nose shape. Although none of the experimental results include the supersonic leading-edge condition, the calculated results are included as a matter of interest.

The results of these calculations are shown in figures 25 and 26 for wings having a uniform thickness ratio of 0.03. The results in figure 25 show the effect of the extent of flat airfoil midsection. The corresponding test models are noted. The results in figure 26 show the effect of decreasing the average airfoil aftersection slopes from those of the basic NACA 0003-63 section. The values of  $h/t$  resulting from this procedure are noted in the figure. For those cases in which a finite thickness at the trailing edge existed, a base drag allowance was included utilizing the base pressure measurements from reference 8.

## REFERENCES

1. Stack, John, and Von Doenhoff, Albert E.: Tests of 16 Related Airfoils at High Speeds. NACA Rep. 492, 1934.
2. Morrow, John D., and Nelson, Robert L.: Large-Scale Flight Measurements of Zero-Lift Drag of 10 Wing-Body Configurations at Mach Numbers From 0.8 to 1.6. NACA RM L52D18a, 1953.
3. Van Driest, E. R.: Turbulent Boundary Layer in Compressible Fluids. Jour. Aero. Sci., vol. 18, no. 3, Mar. 1951, pp. 145-160, 216.
4. Morrow, John D., and Katz, Ellis: Flight Investigation at Mach Numbers From 0.6 to 1.7 To Determine Drag and Base Pressures on a Blunt-Trailing-Edge Airfoil and Drag of Diamond and Circular-Arc Airfoils at Zero Lift. NACA RM L50E19a, 1950.
5. Fraenkel, L. E.: The Theoretical Wave Drag of Some Bodies of Revolution. Rep. No. Aero 2420, British R.A.E., May 1951.
6. Beane, Beverly: The Characteristics of Supersonic Wings Having Biconvex Sections. Jour. Aero. Sci., vol. 18, no. 1, Jan. 1951, pp. 7-20.
7. Puckett, Allen E.: Supersonic Wave Drag of Thin Airfoils. Jour. Aero. Sci., vol. 13, no. 9, Sept. 1946, pp. 475-484.
8. Love, Eugene S.: The Base Pressure at Supersonic Speeds on Two-Dimensional Airfoils and Bodies of Revolution (With and Without Fins) Having Turbulent Boundary Layers. NACA RM L53C02, 1953.

~~CONFIDENTIAL~~

TABLE I  
FUSELAGE ORDINATES

Distance from nose of fuselage, in.	Fuselage radius, in.
0	0
.390	.097
.585	.145
.975	.239
1.950	.469
3.900	.902
5.850	1.298
7.800	1.658
11.700	2.267
15.600	2.730
19.500	3.047
23.400	3.218
27.300	3.248
31.200	3.221
35.100	3.161
39.000	3.069
42.900	2.943
46.800	2.785
50.700	2.594
54.600	2.371
58.500	2.115
62.400	1.826
65.000	1.615

TABLE II  
TEST CONFIGURATIONS

Model	Aspect ratio	$\Delta_{LE}$ , deg	$\Delta_{TE}$ , deg	$c_f/c$	h/t	$\bar{c}$ , ft	NACA airfoil section			
							Theoretical root		0.9 theoretical semispan	
							0 to 0.3c	0.3c to 1.0c	0 to 0.3c	0.3c to 1.0c
1	2.06	60	0	0	0	2.419	0003-03		0006-03	
2	2.06	60	0	0	0	2.419	0003-33		0006-33	
3	2.06	60	0	0	0	2.419	0003-63		0006-63	
4	2.06	60	0	0	0	2.419	0003-93		0006-93	
5	2.06	60	0	0.2	0	2.419	0003-63	See fig. 4	0006-63	See fig. 4
6	2.06	60	0	0.4	0	2.419	0003-63	See fig. 4	0006-63	See fig. 4
7	2.06	60	0	0.5	0	2.419	0003-63	See fig. 4	0006-63	See fig. 4
8	2.06	60	0	0.7	1.0	2.419	0003-63	See fig. 4	0006-63	See fig. 4
9	2.06	60	0	0	0.3	2.419	0003-63	See fig. 4	0006-63	See fig. 4
10	3.45	60	34.7	0	0	1.452	See fig. 5		See fig. 5	
11	2.06	60	0	0	0	2.419	65A003		65A003	
12 (fig. 6)	2.06	60	0	0	0	2.419	0003-63		0006-63	

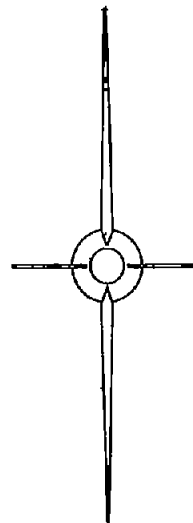
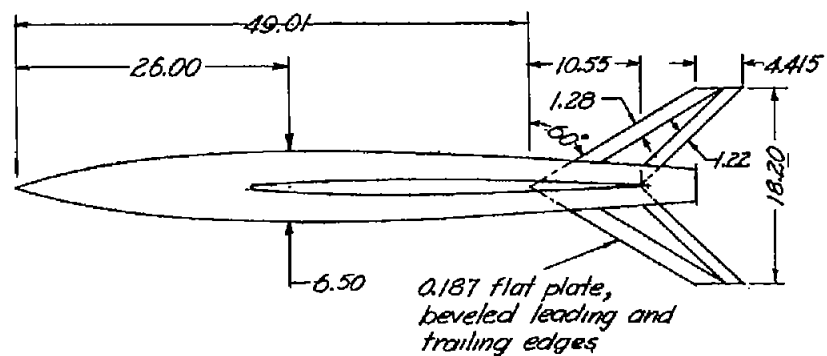
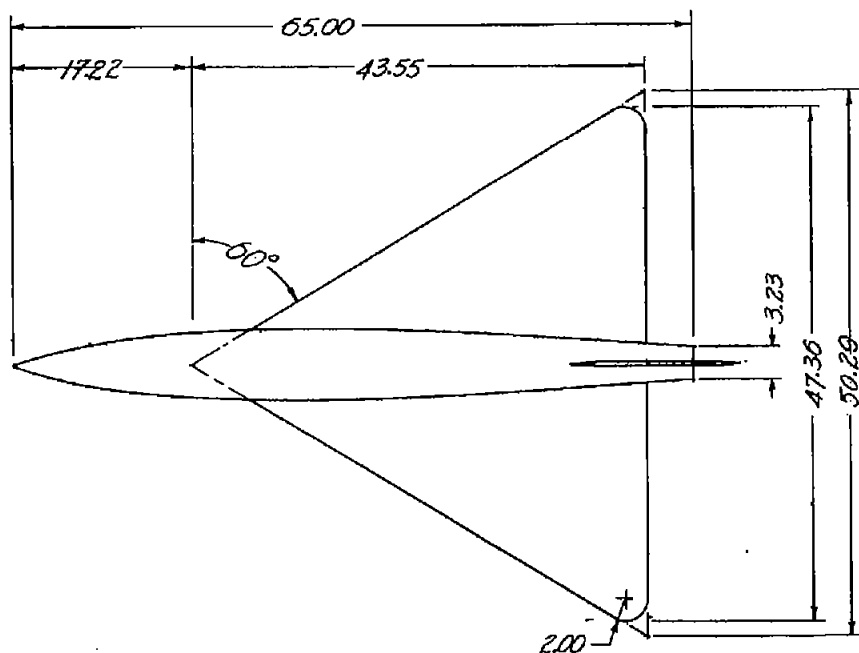
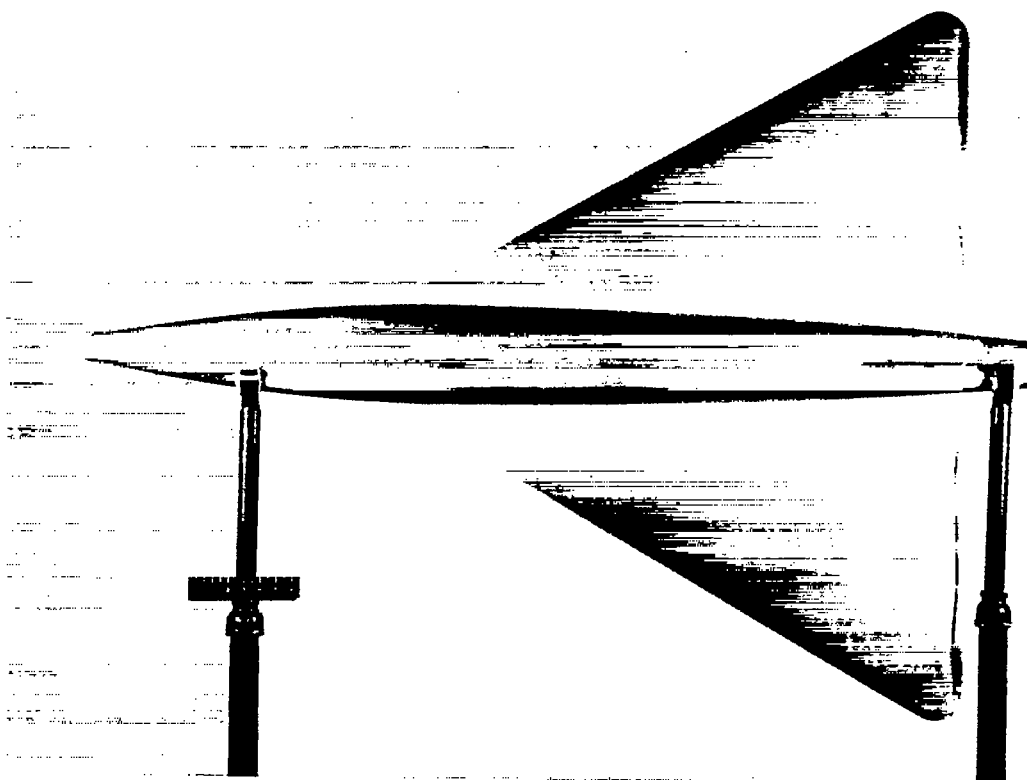
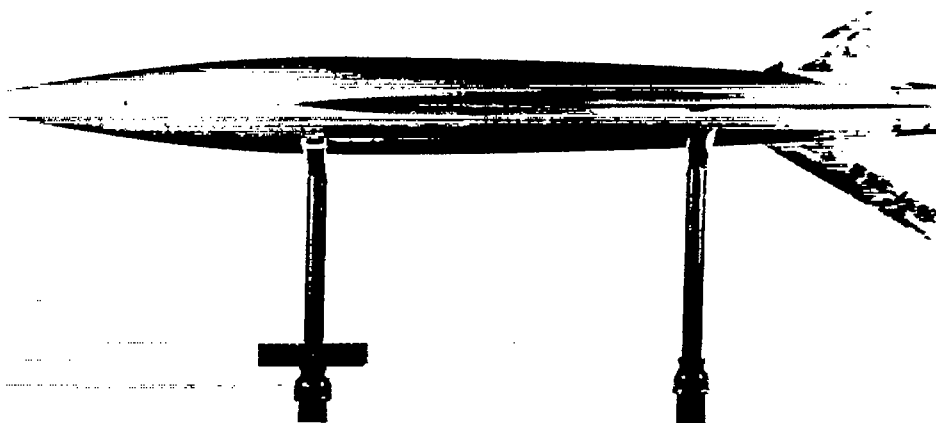


Figure 1.- General arrangement. Dimensions are in inches.



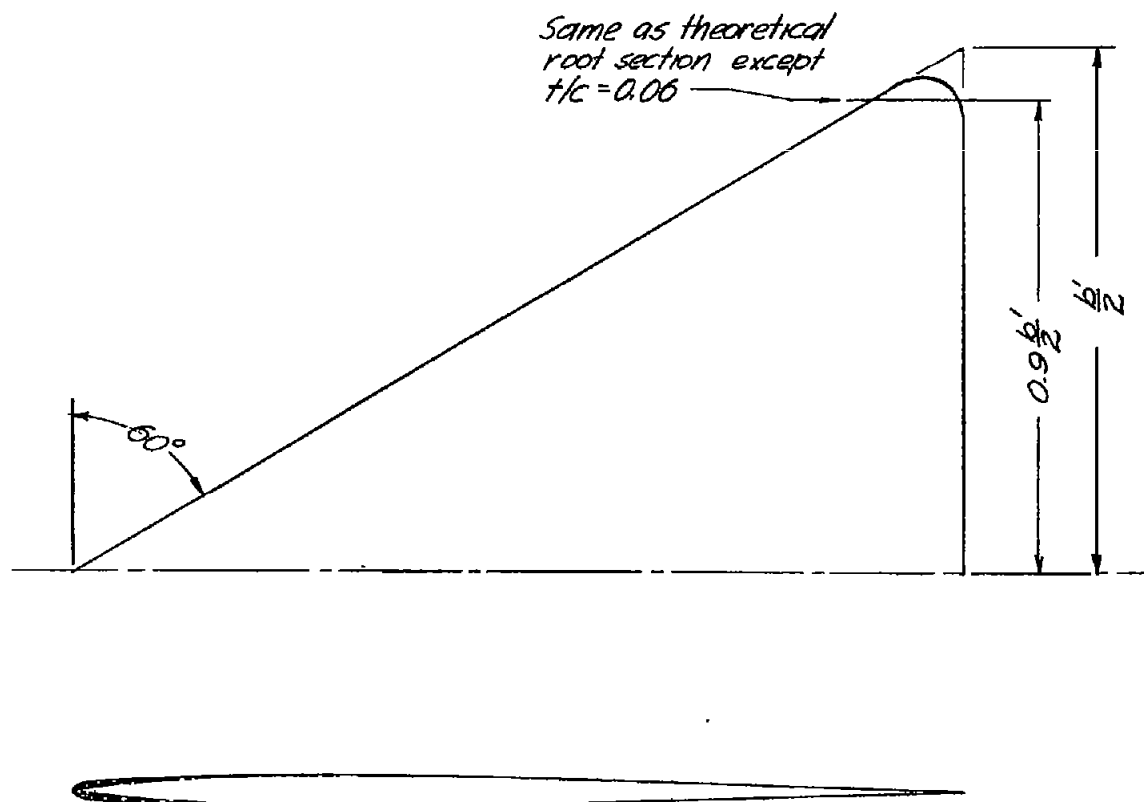


L-77995



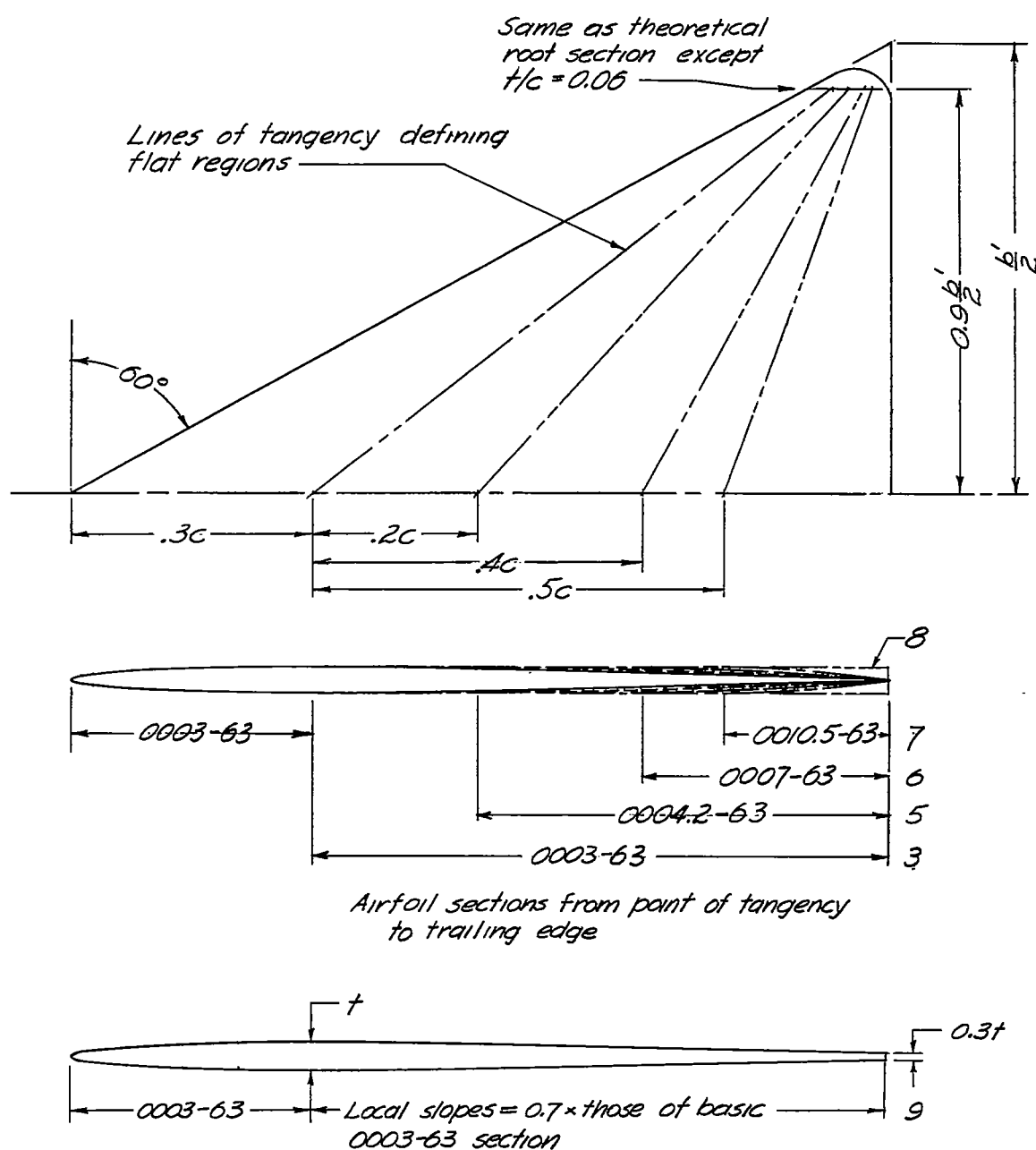
L-77996

Figure 2.- Photographs of typical model.



Model	Theoretical root section	Leading-edge radius, percent $c$
1	0003-03	0
2	0003-33	.025
3	0003-63	.100
4	0003-93	.300

Figure 3.- Geometry of wings used in investigation of leading-edge effects.



Theoretical root sections

Figure 4.- Geometry of wings used in investigation of trailing-edge effects.  
Numbers denote models.

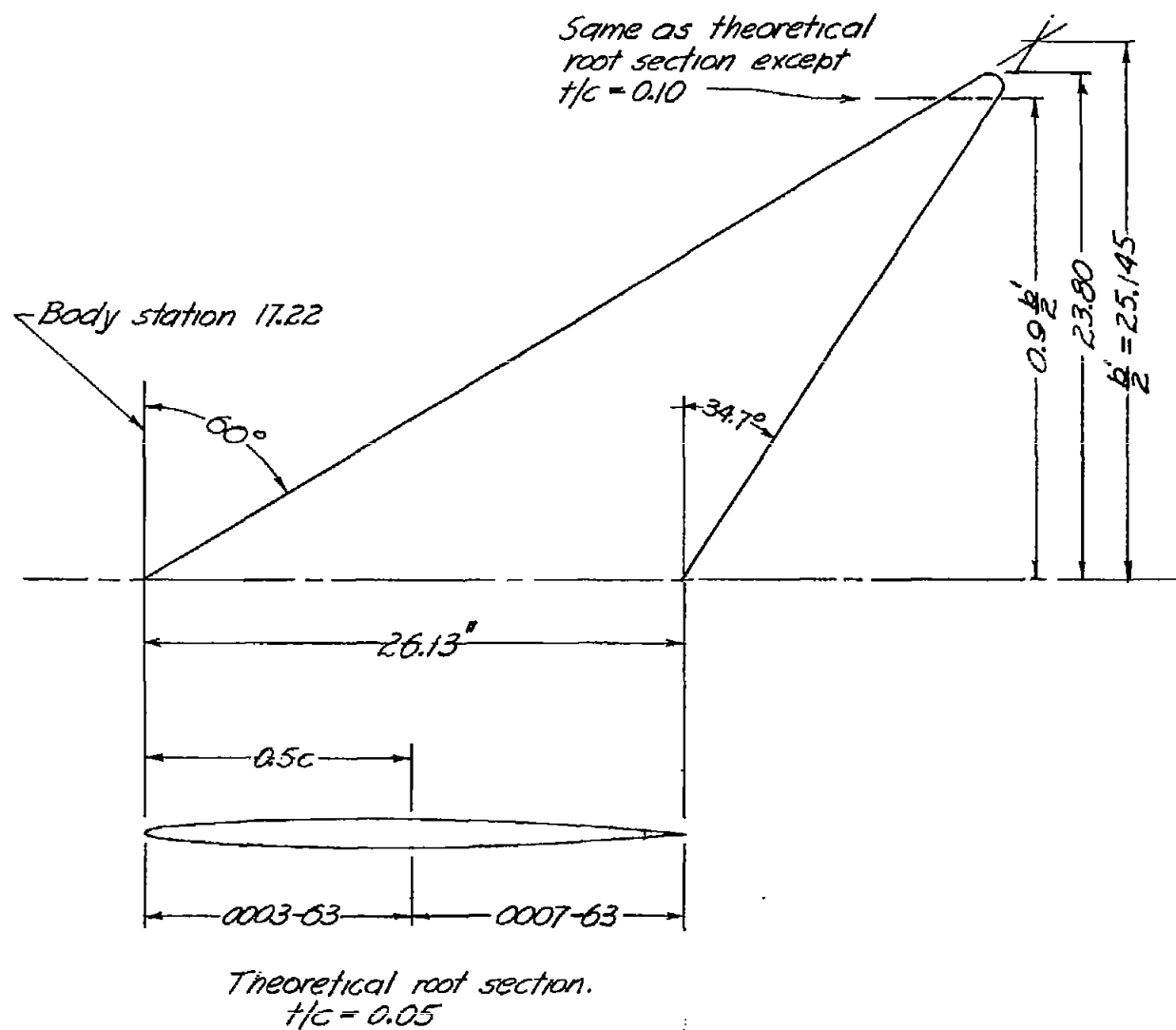
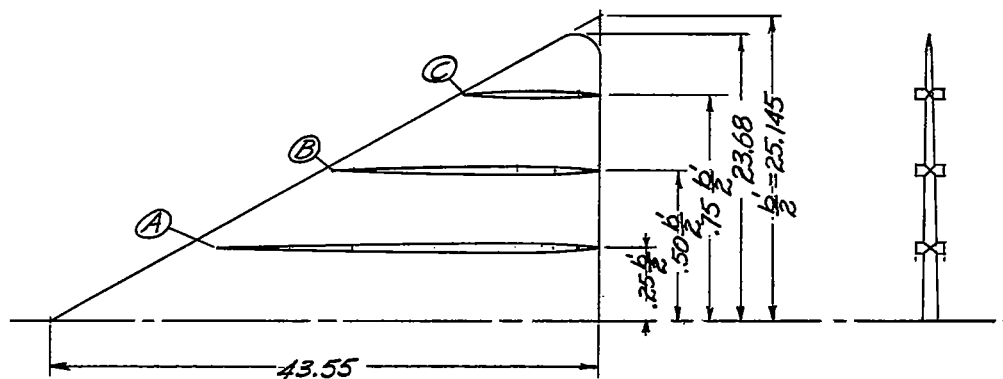
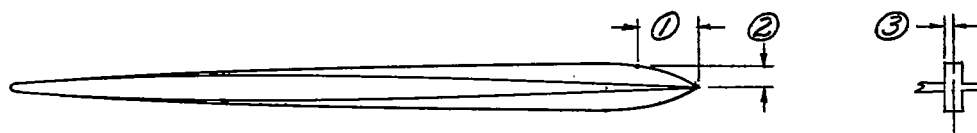


Figure 5.- Geometry of notched delta wing. Model 10.



Airfoil section at theoretical root ----- 0003-63

Airfoil section at  $.9\frac{1}{16}$  station ----- 0006-63



Typical sections through simulated control-actuator housings.

Housing A			Housing B			Housing C		
1	2	3	1	2	3	1	2	3
0	0	0	0	0	0	0	0	0
.871	.409	.137	.871	.409	.137	.871	.409	.137
1.742	.728	.243	1.742	.728	.243	1.742	.728	.243
2.613	.956	.319	2.613	.956	.319	2.613	.956	.319
3.484	1.092	.364	3.484	1.092	.364	3.484	1.092	.364
4.355	1.138	.379	4.355	1.138	.379	4.355	1.138	.379
6.532	1.132	.377	6.532	1.122	.378	5.444	1.107	.369
9.799	1.104	.362	8.710	1.073	.353	6.533	1.015	.336
13.065	1.050	.336	10.888	.992	.321	7.621	.860	.283
16.331	.972	.298	13.065	.878	.276	8.710	.644	.208
19.576	.868	.247	15.242	.732	.217	9.799	.366	.111
22.864	.741	.185	17.420	.553	.146	10.343	.204	.055
24.497	.667	.149	19.598	.342	.062	10.779	.063	.066
26.130	.588	.110	20.686	.224	.015	10.833	.045	0
27.763	.502	.068	21.013	.187	0			
29.396	.410	.024						
30.213	.362	0						

Figure 6.- Geometry of wing of model 12. Dimensions are in inches.

CONFIDENTIAL

NACA RM L53L24a

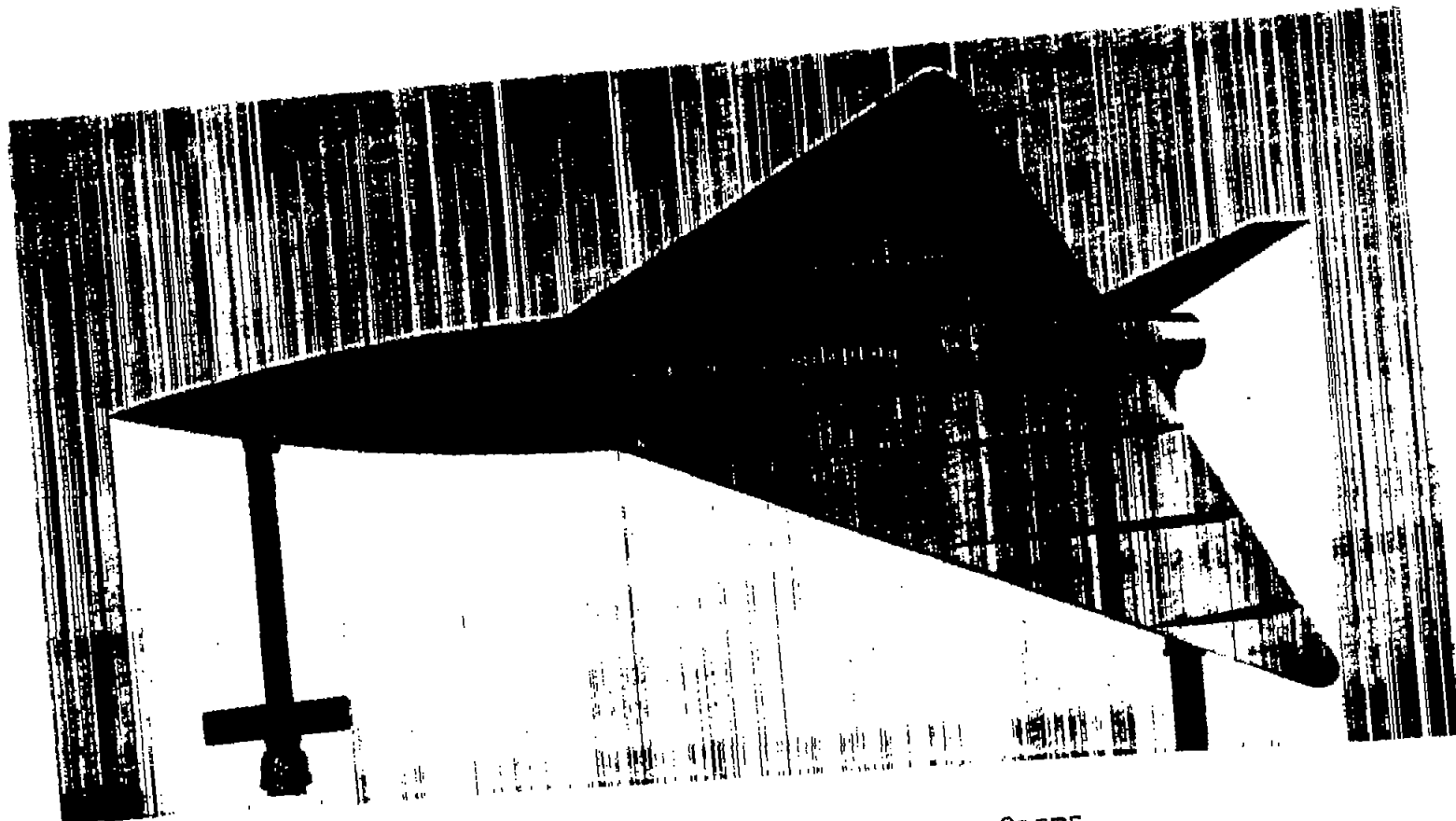


Figure 7.- Model 12.

L-81575

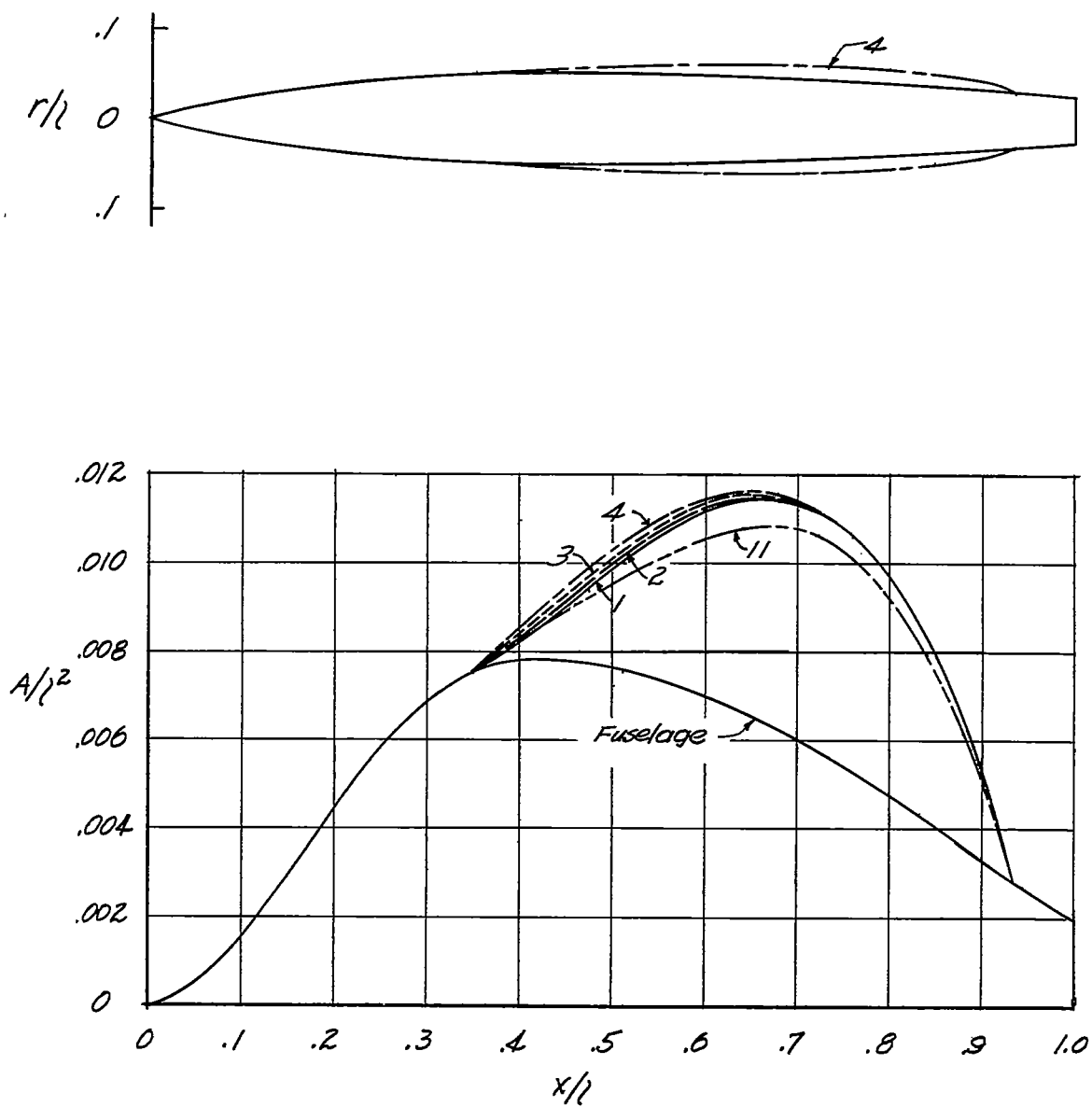


Figure 8.- Longitudinal distributions of cross-sectional area. Numbers denote models.

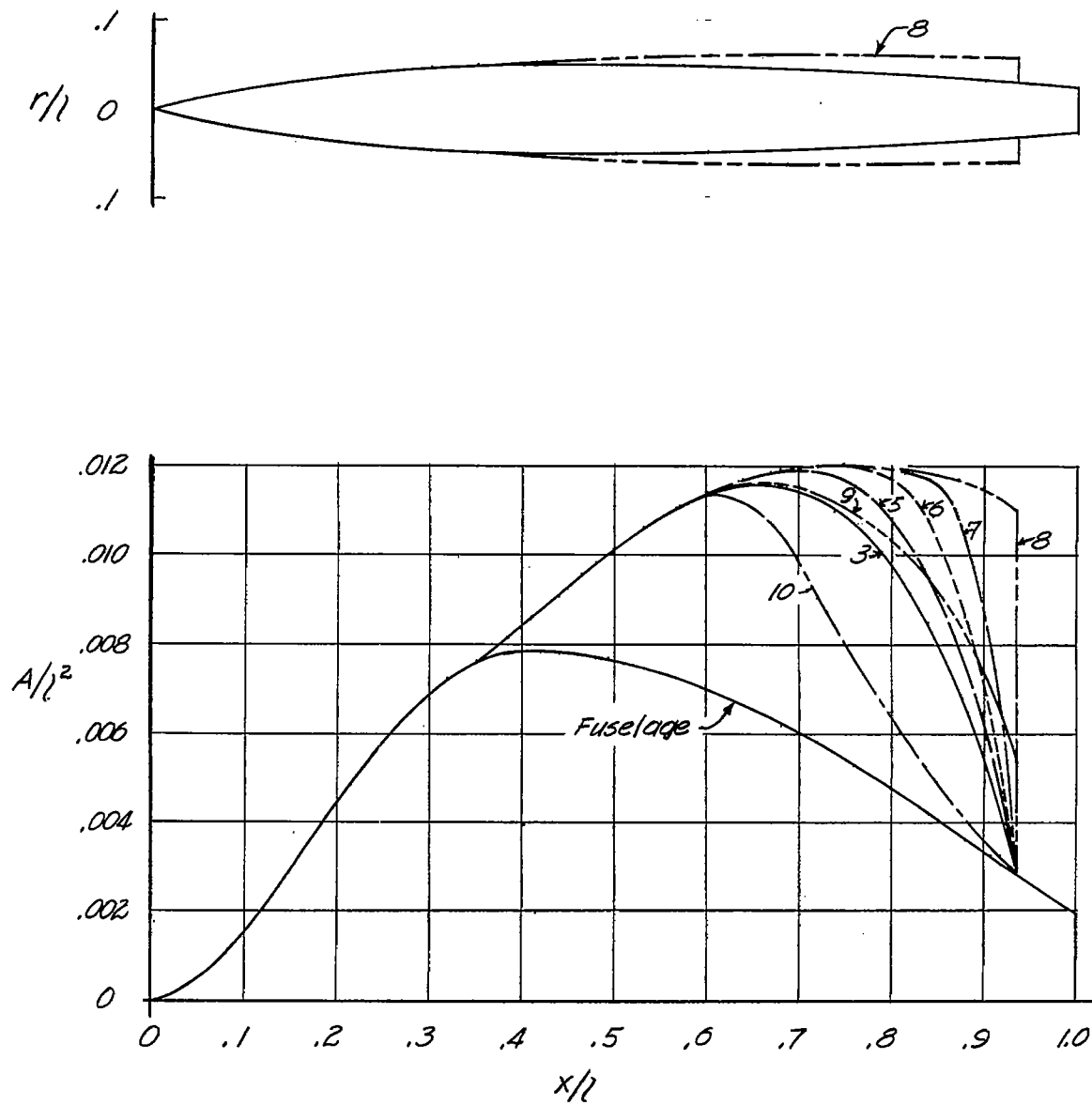
~~CONFIDENTIAL~~

Figure 9.- Longitudinal distributions of cross-sectional area. Numbers denote models.

~~CONFIDENTIAL~~



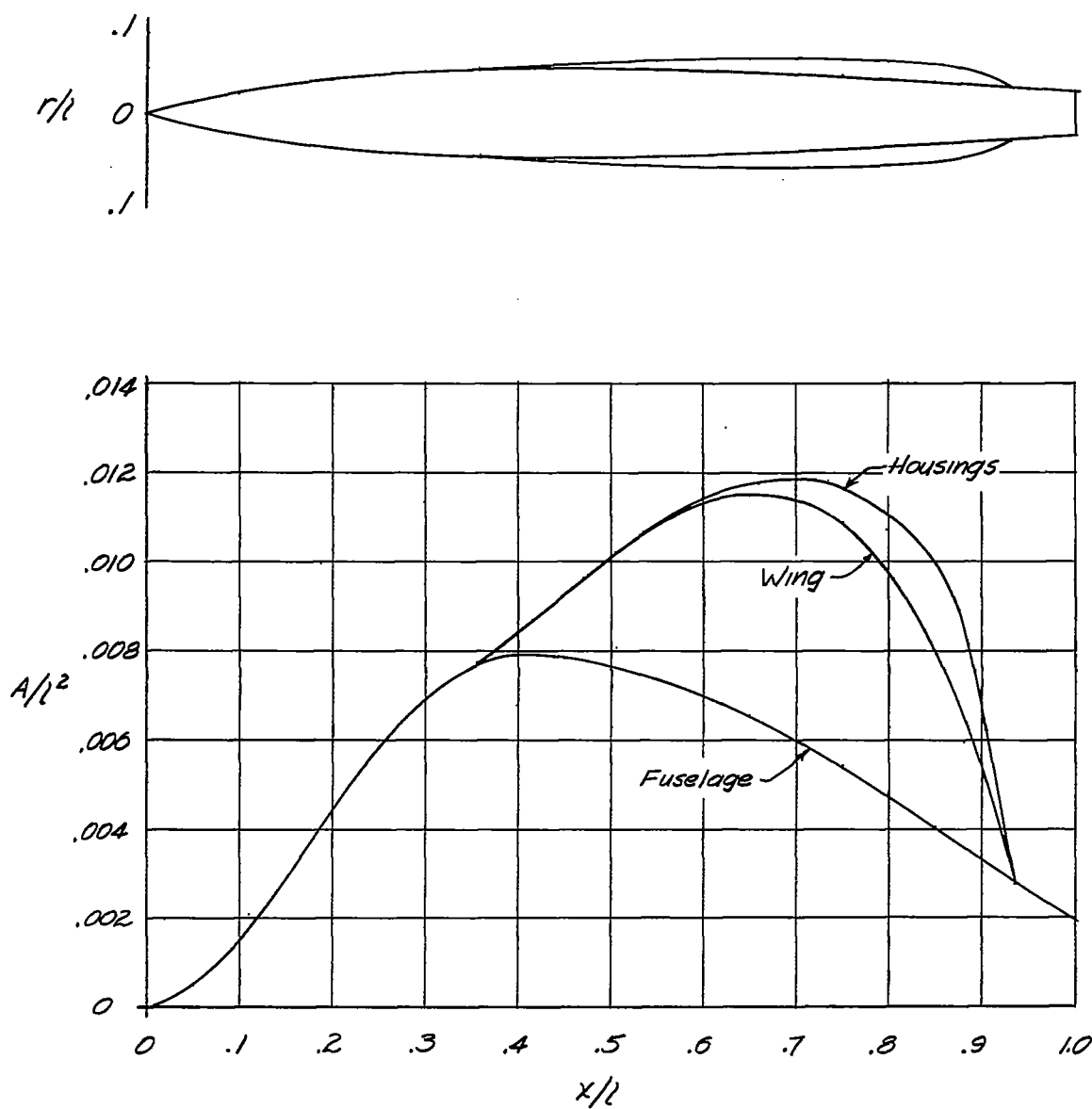


Figure 10.- Longitudinal distribution of cross-sectional area. Model 12.

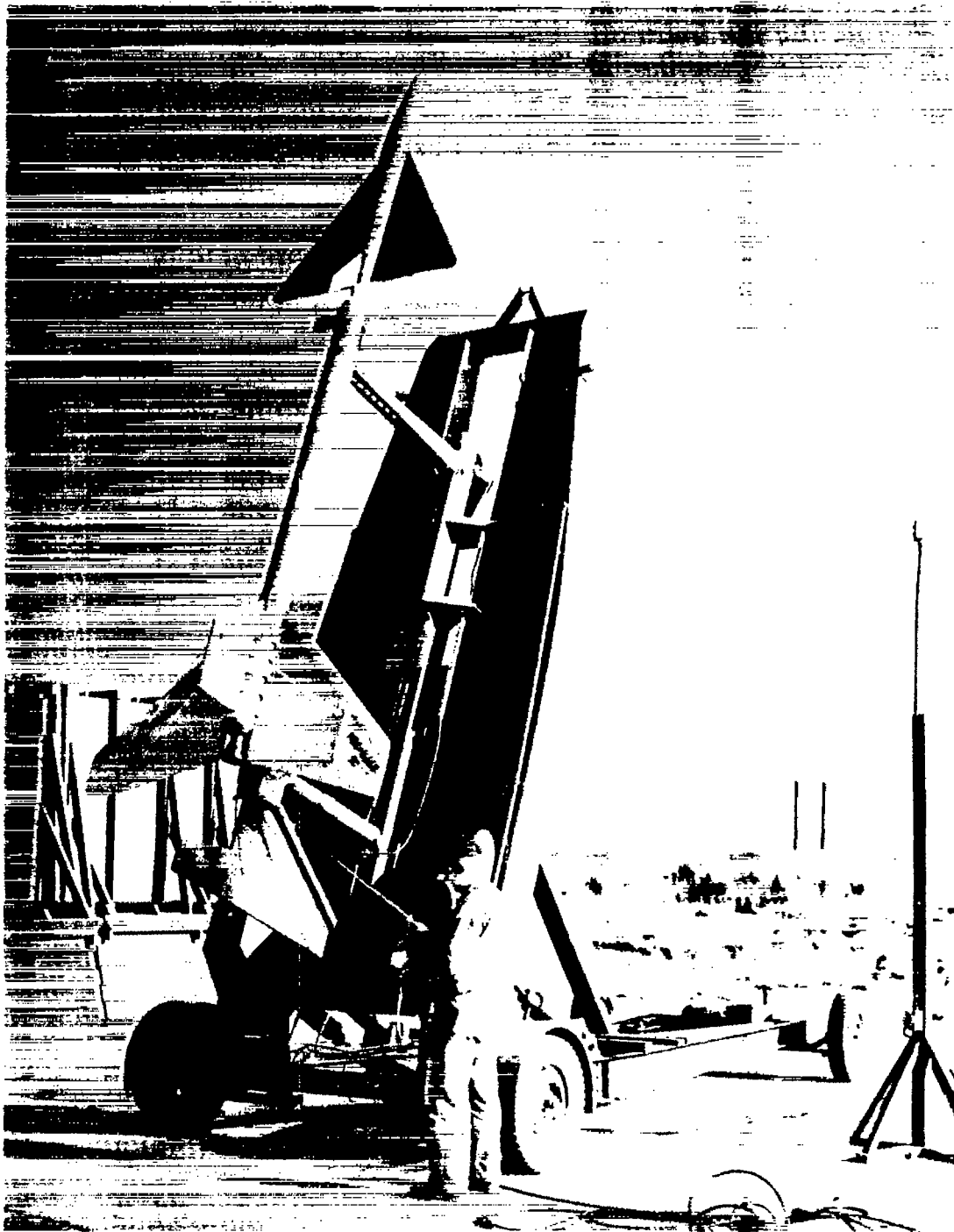


Figure 11.- Model-booster-launcher assembly.

L-78633

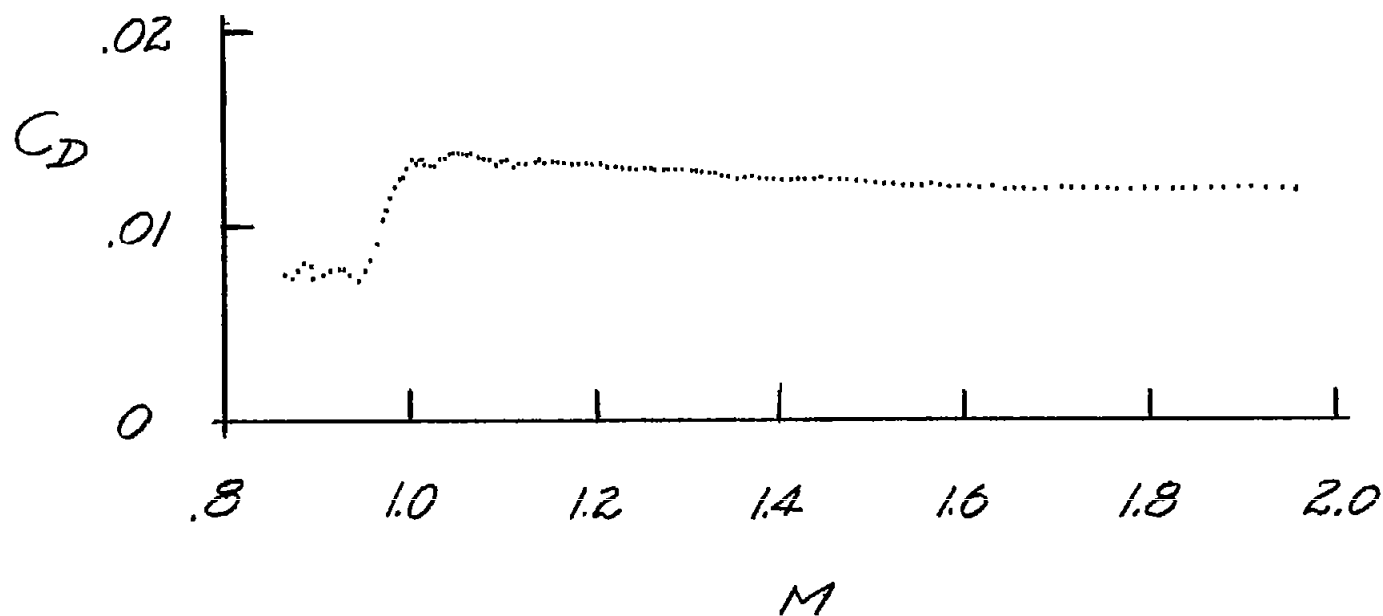


Figure 12.- Typical set of test results. Model 1.

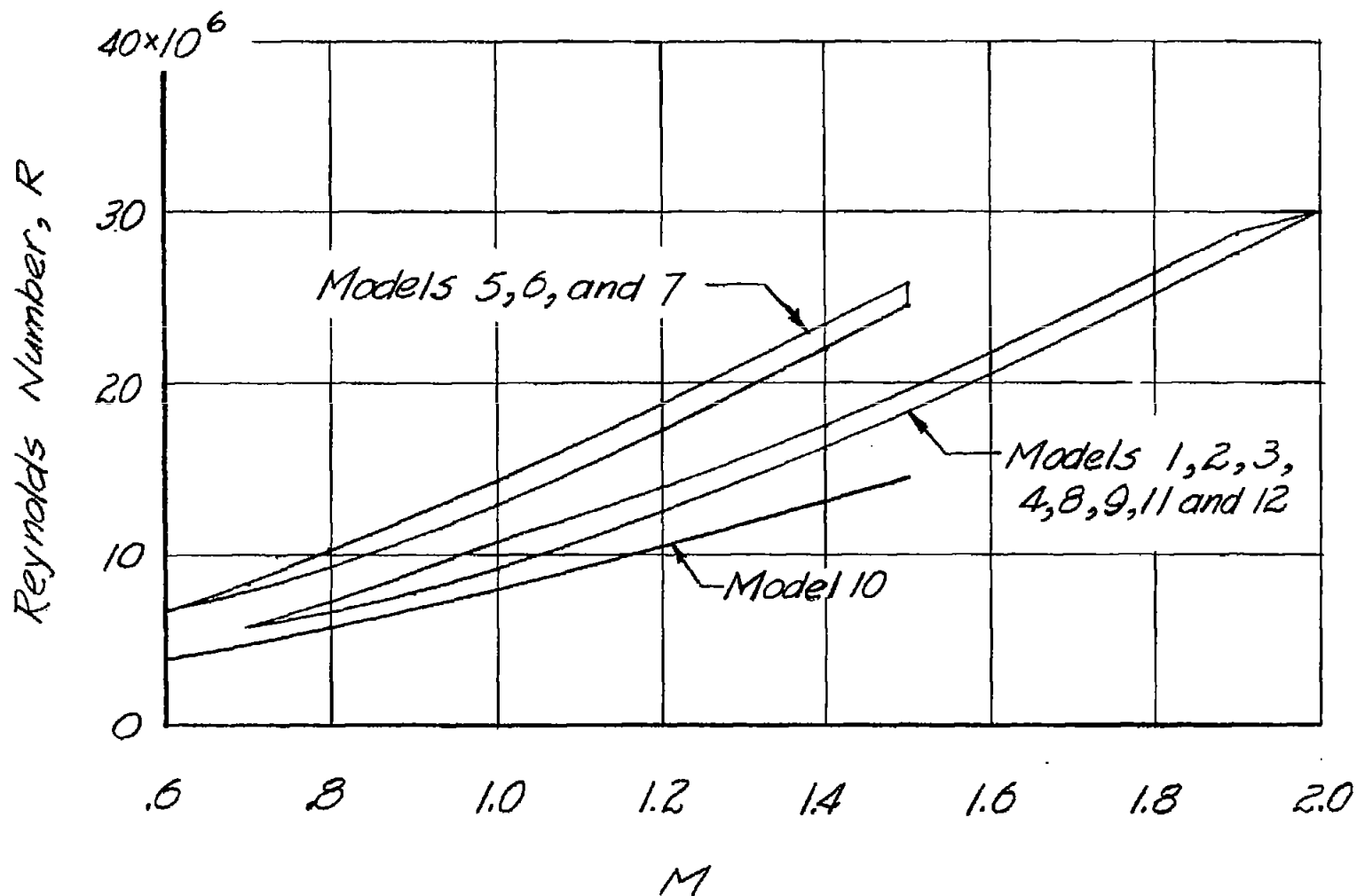
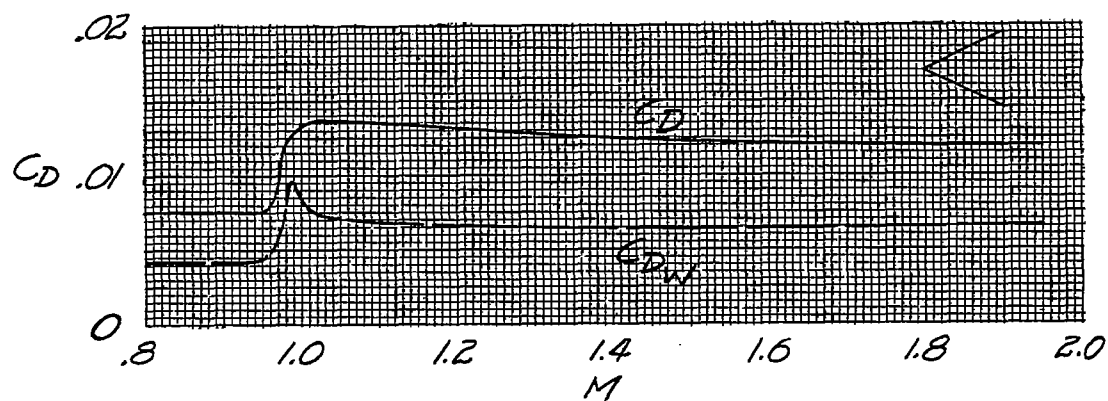
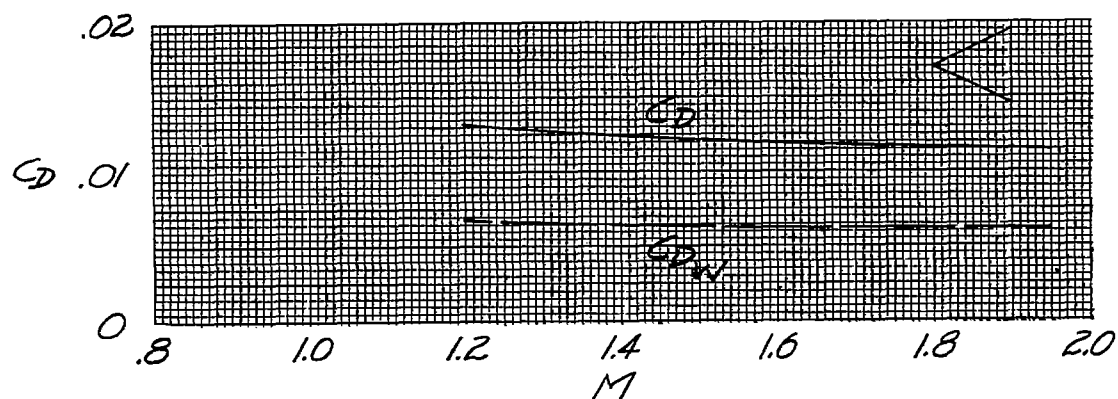


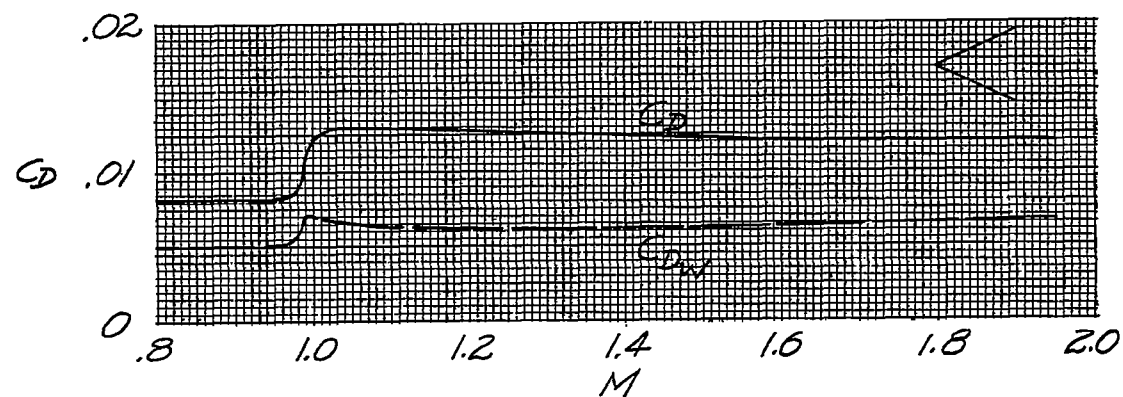
Figure 13.- Reynolds numbers of tests.



(a) Model 1.

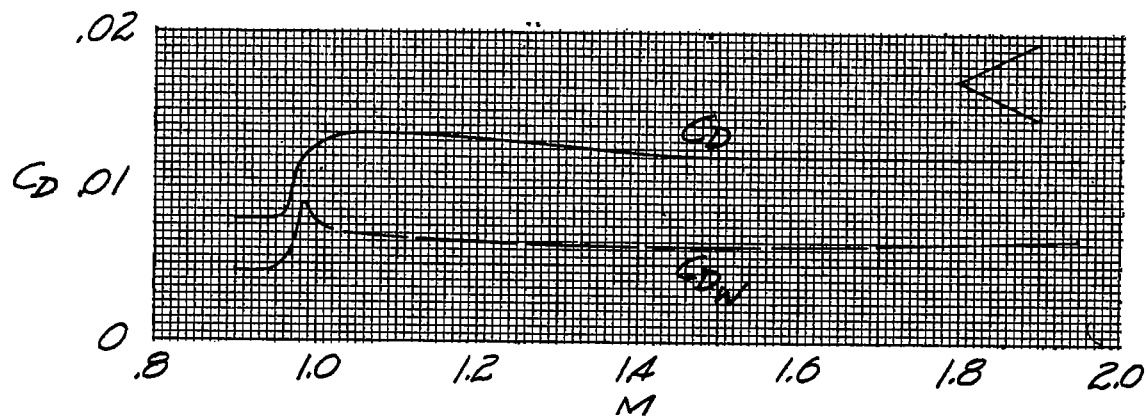


(b) Model 2.

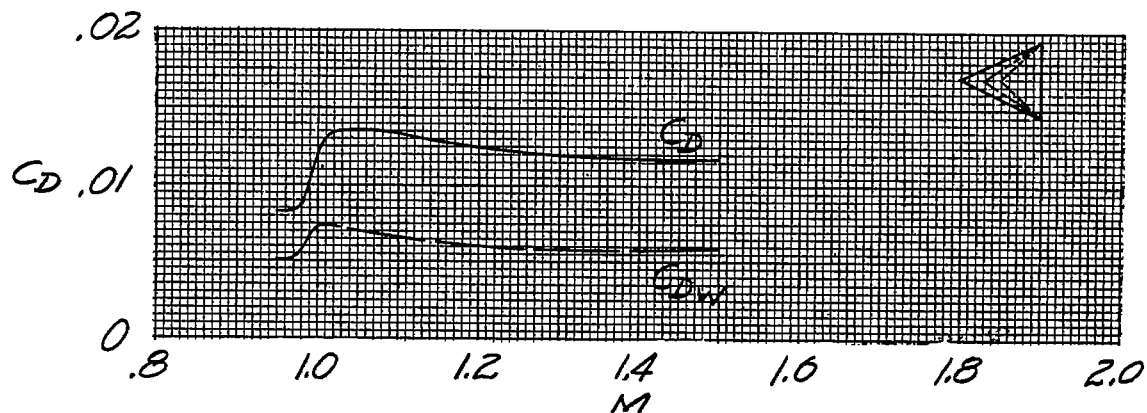


(c) Model 3.

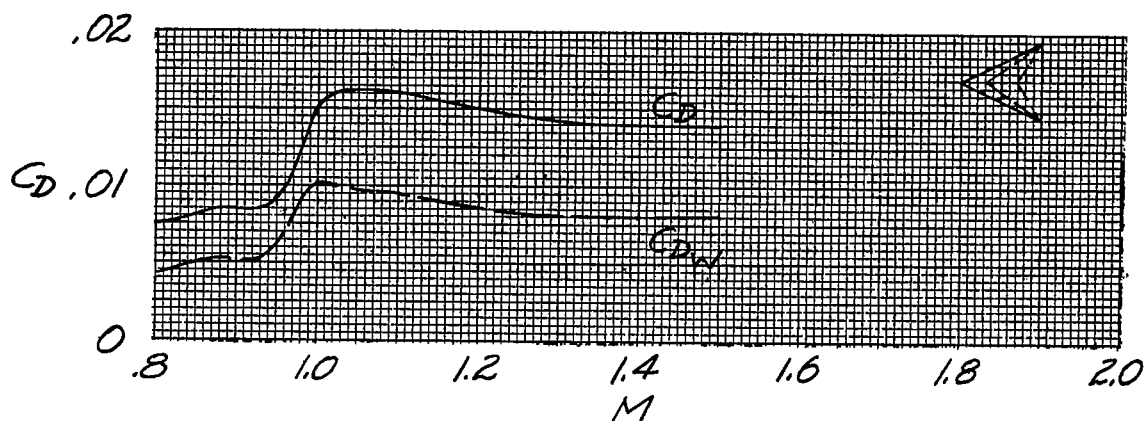
Figure 14.- Test results.



(d) Model 4.

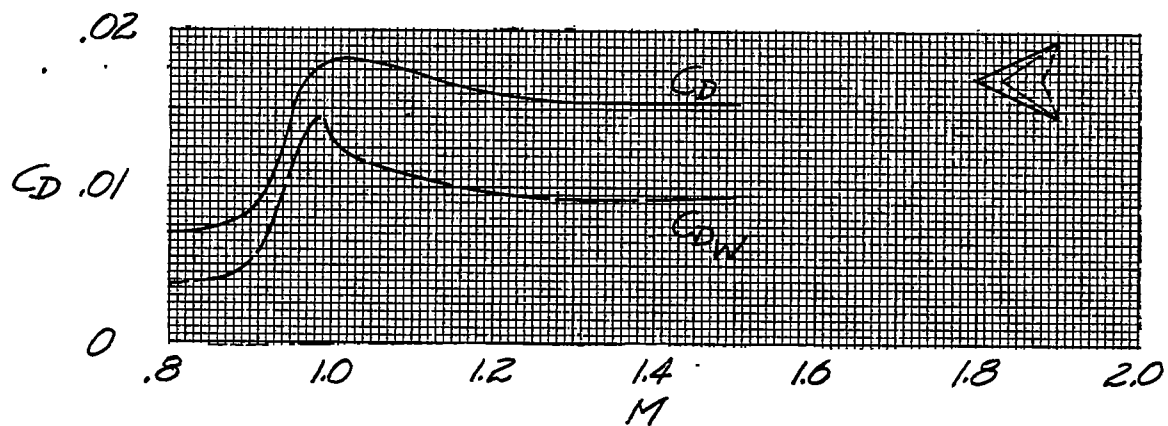


(e) Model 5.

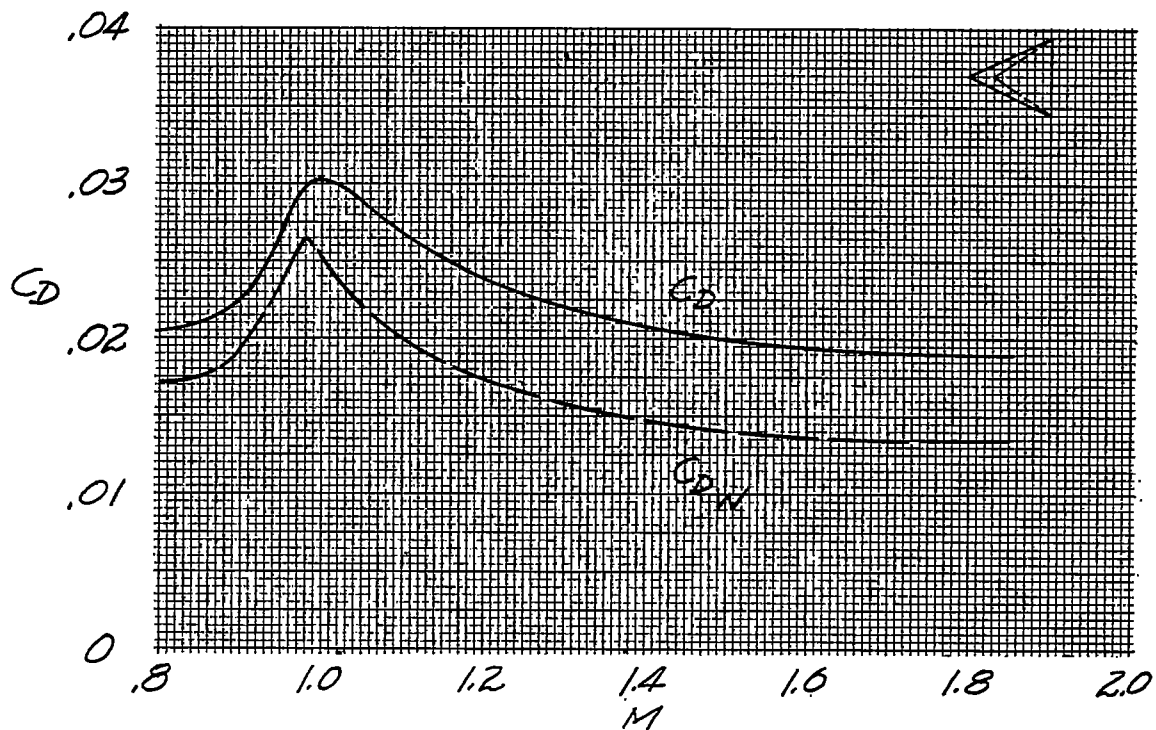


(f) Model 6.

Figure 14.- Continued.

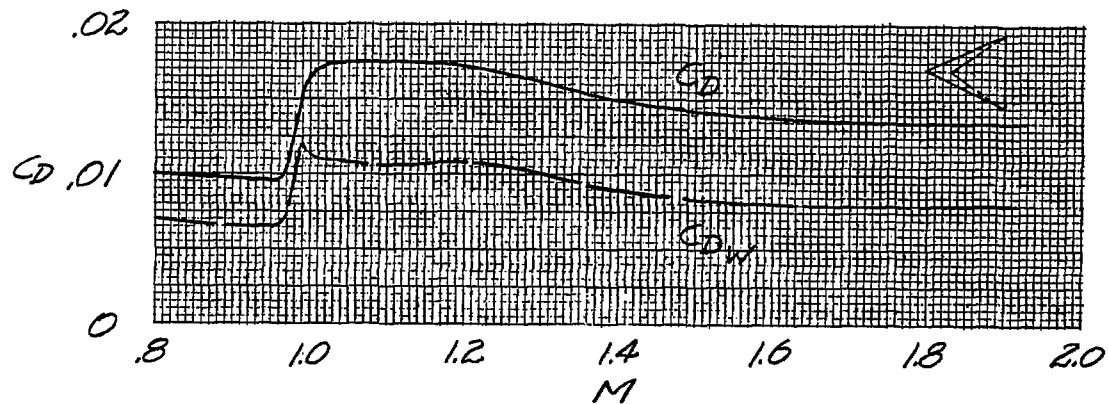


(g) Model 7.

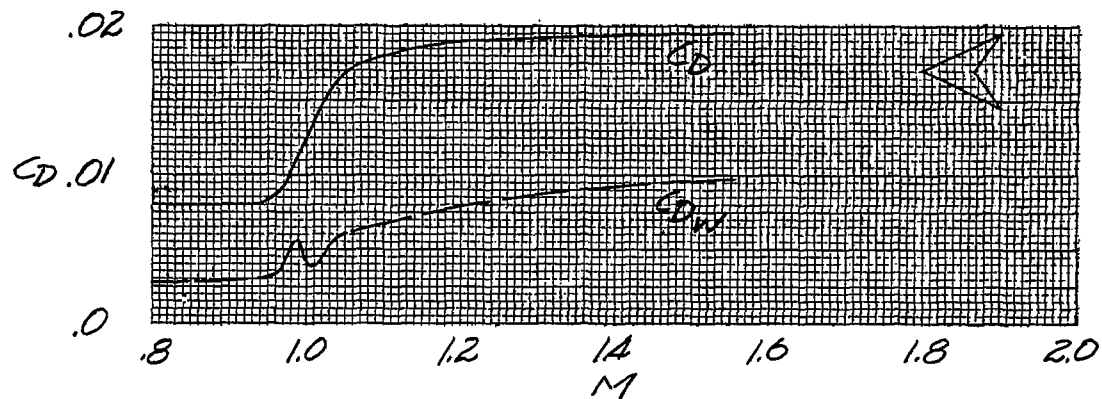


(h) Model 8.

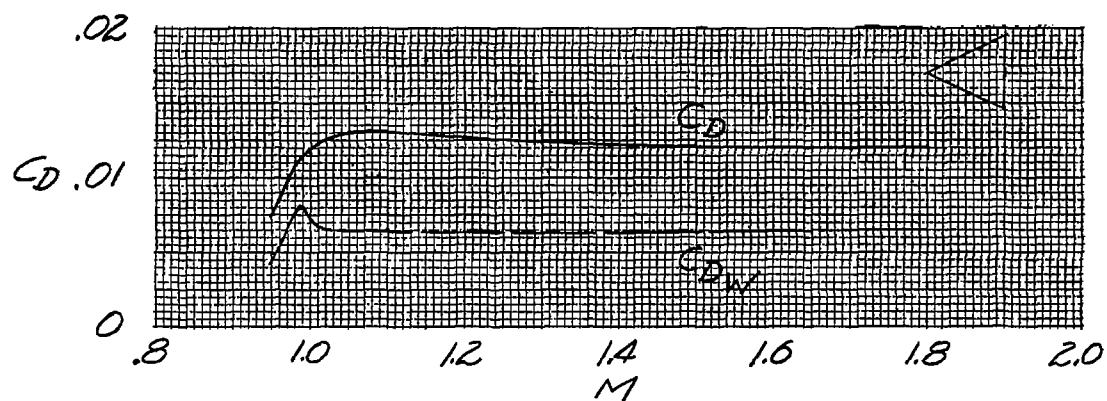
Figure 14.- Continued.



(i) Model 9.



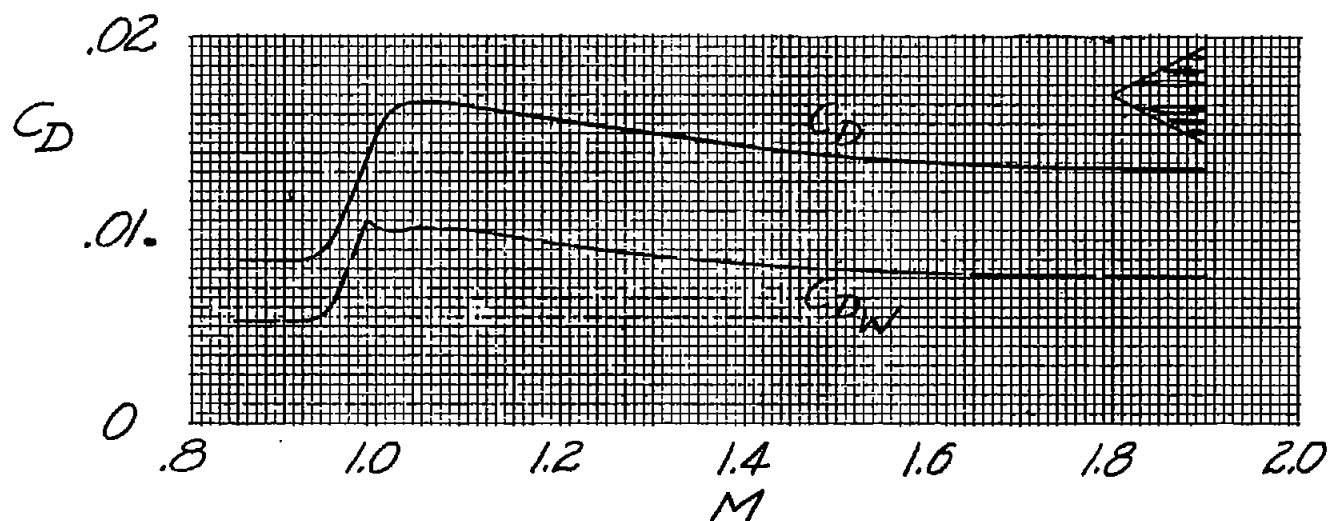
(j) Model 10.



(k) Model 11.

Figure 14.- Continued.





(1) Model 12. Simulated control-actuator housings.

Figure 14.- Concluded.

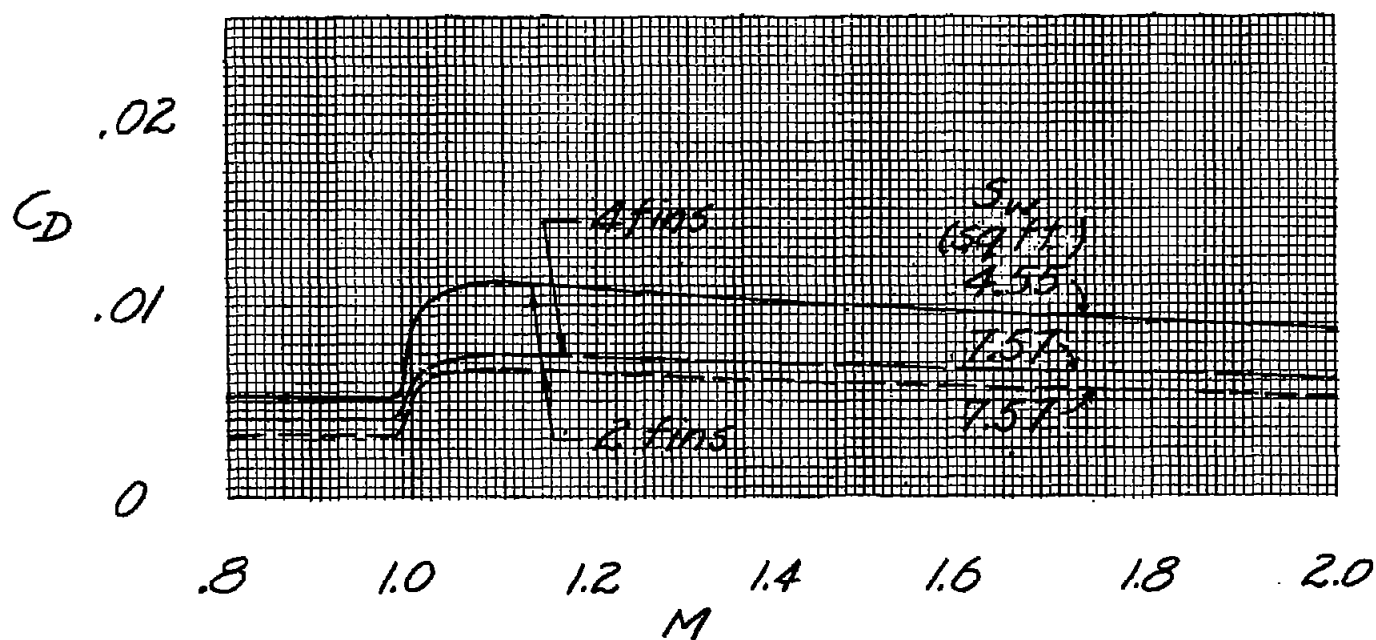


Figure 15.- Body drag.

Model	Airfoil section		
	Root	$0.9 \frac{b'}{2}$	
1	0003-03	0006-03	_____
2	0003-33	0006-33	_____
3	0003-63	0006-63	_____
4	0003-93	0006-93	_____

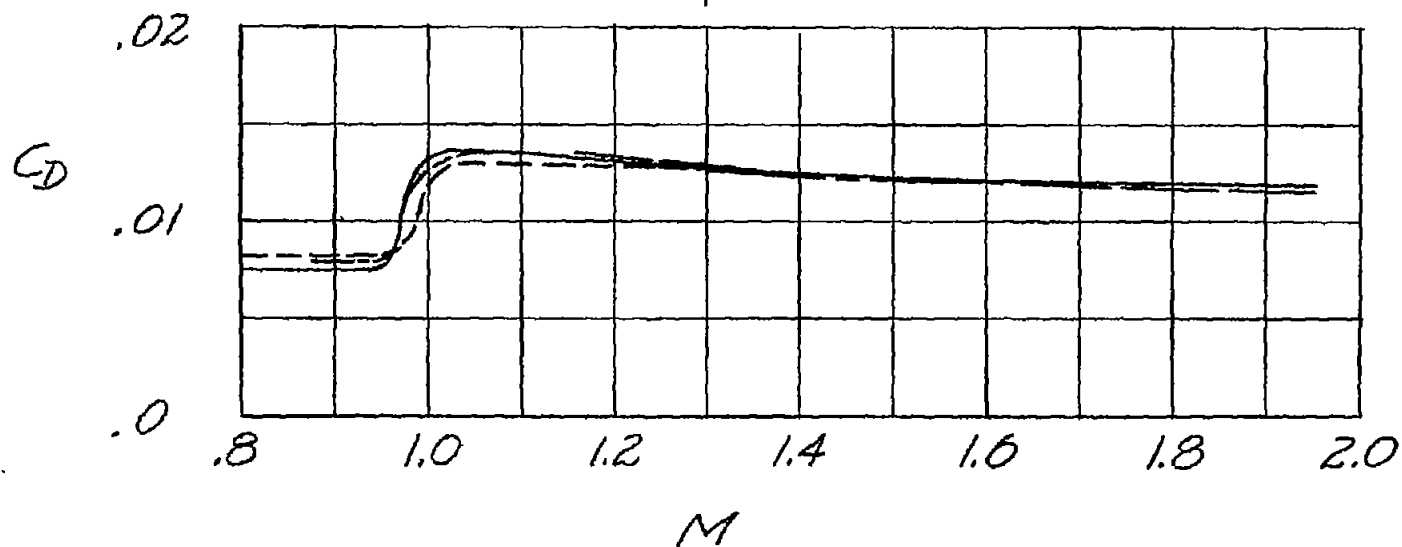


Figure 16.- Effect of leading-edge radius.

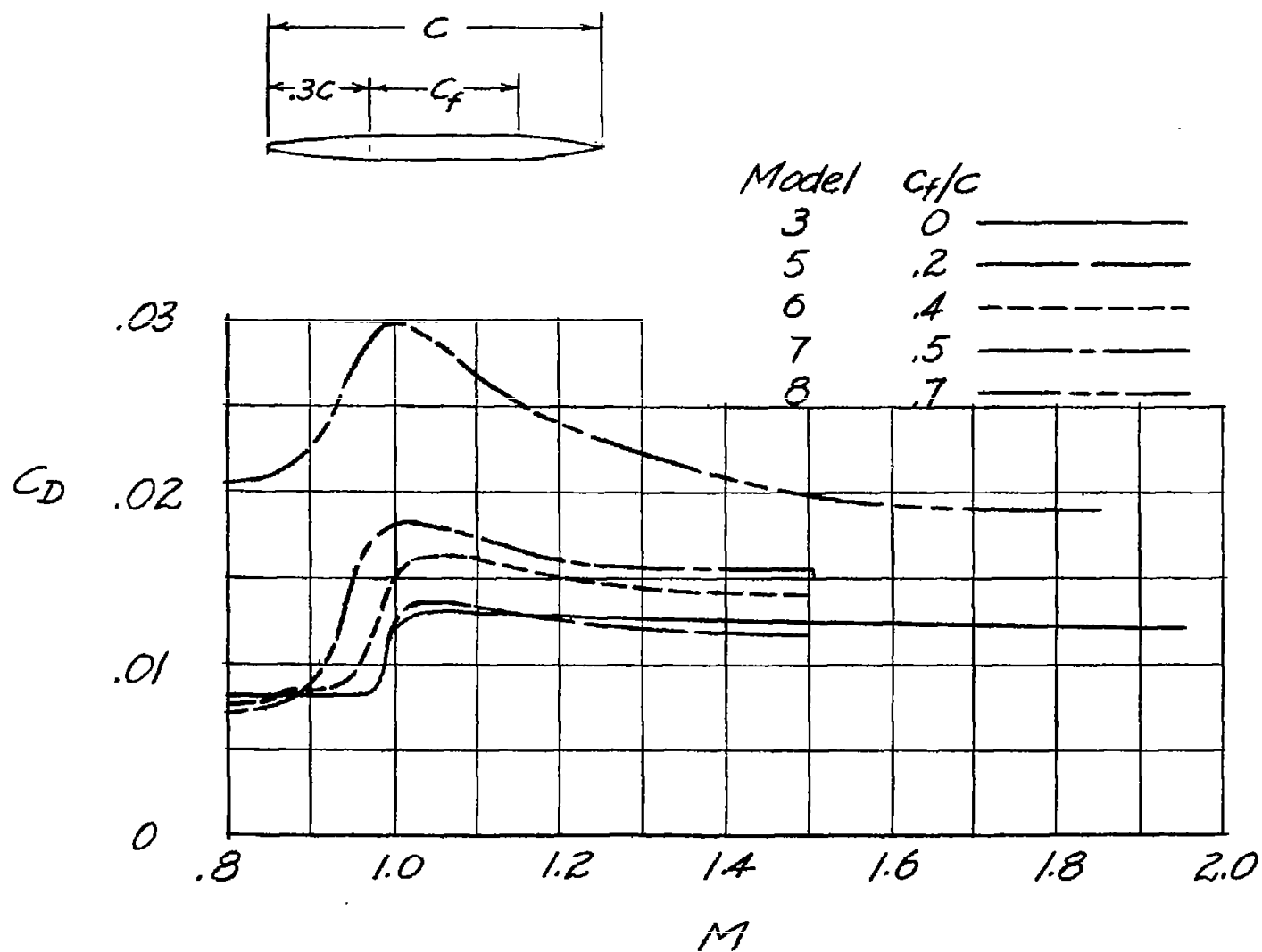
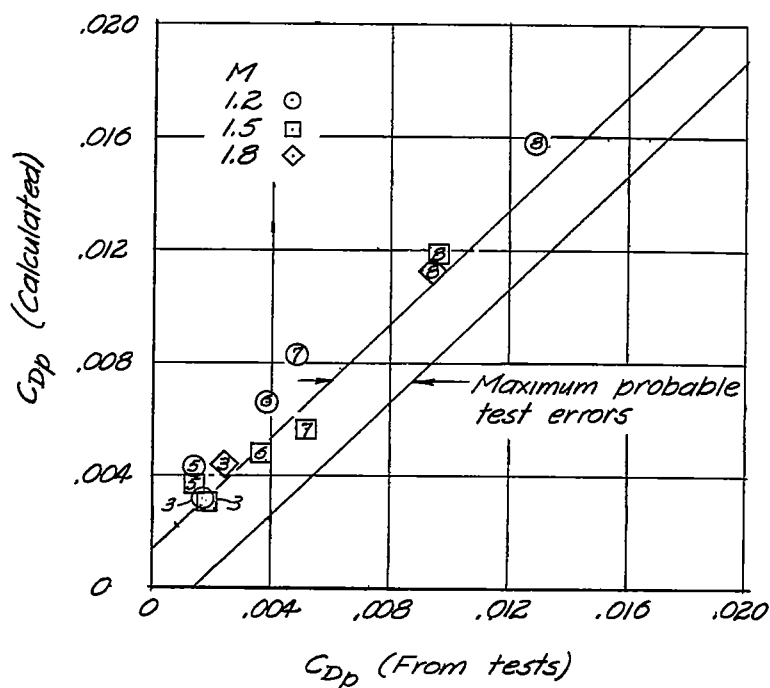
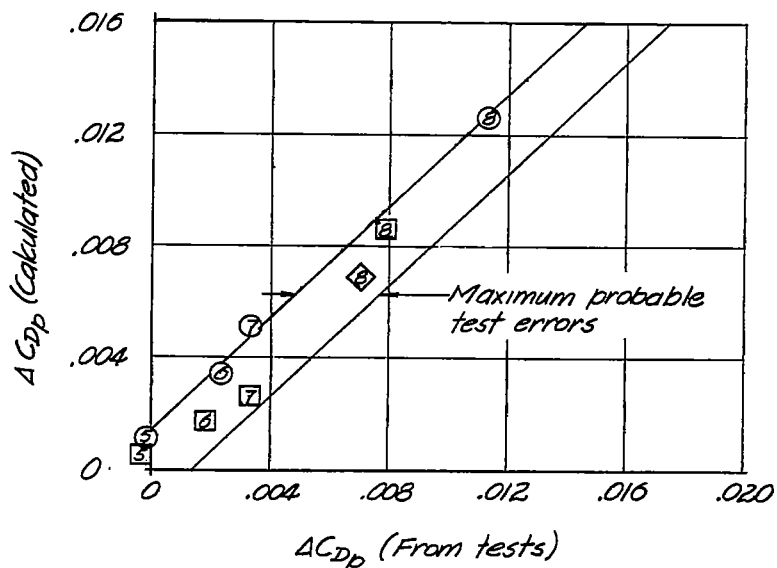


Figure 17.- Effect of flat extent.



(a) Total drag coefficients.



(b) Incremental drag coefficients measured from those of the unmodified section (model 3).

Figure 18.- Comparison of experimentally derived and calculated pressure drag coefficients for series of wings in which extent of flat mid-section is varied. Numbers denote models.

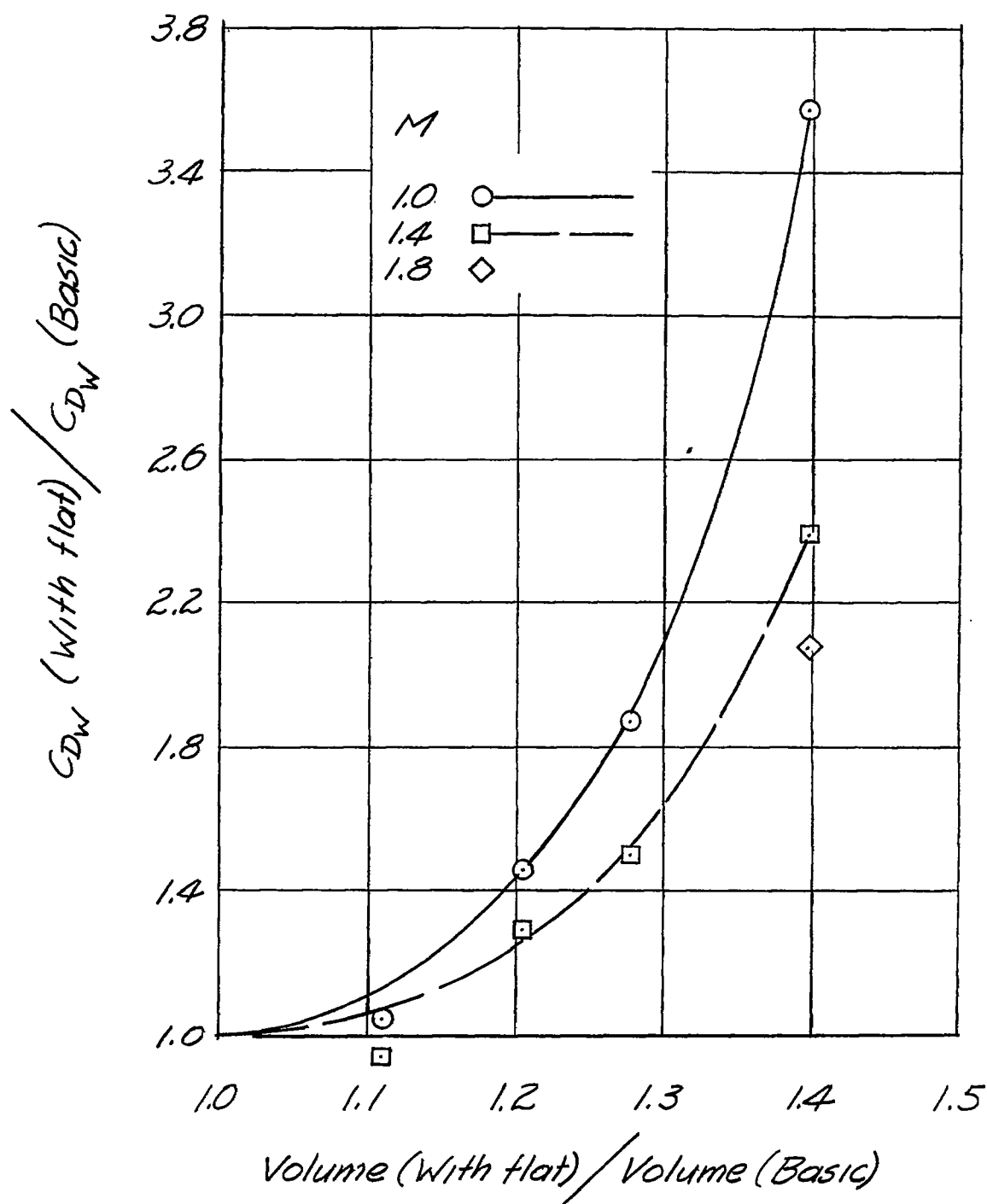


Figure 19.- Variation of relative wing drag with relative wing volume for series of wings in which extent of flat midsection is varied.

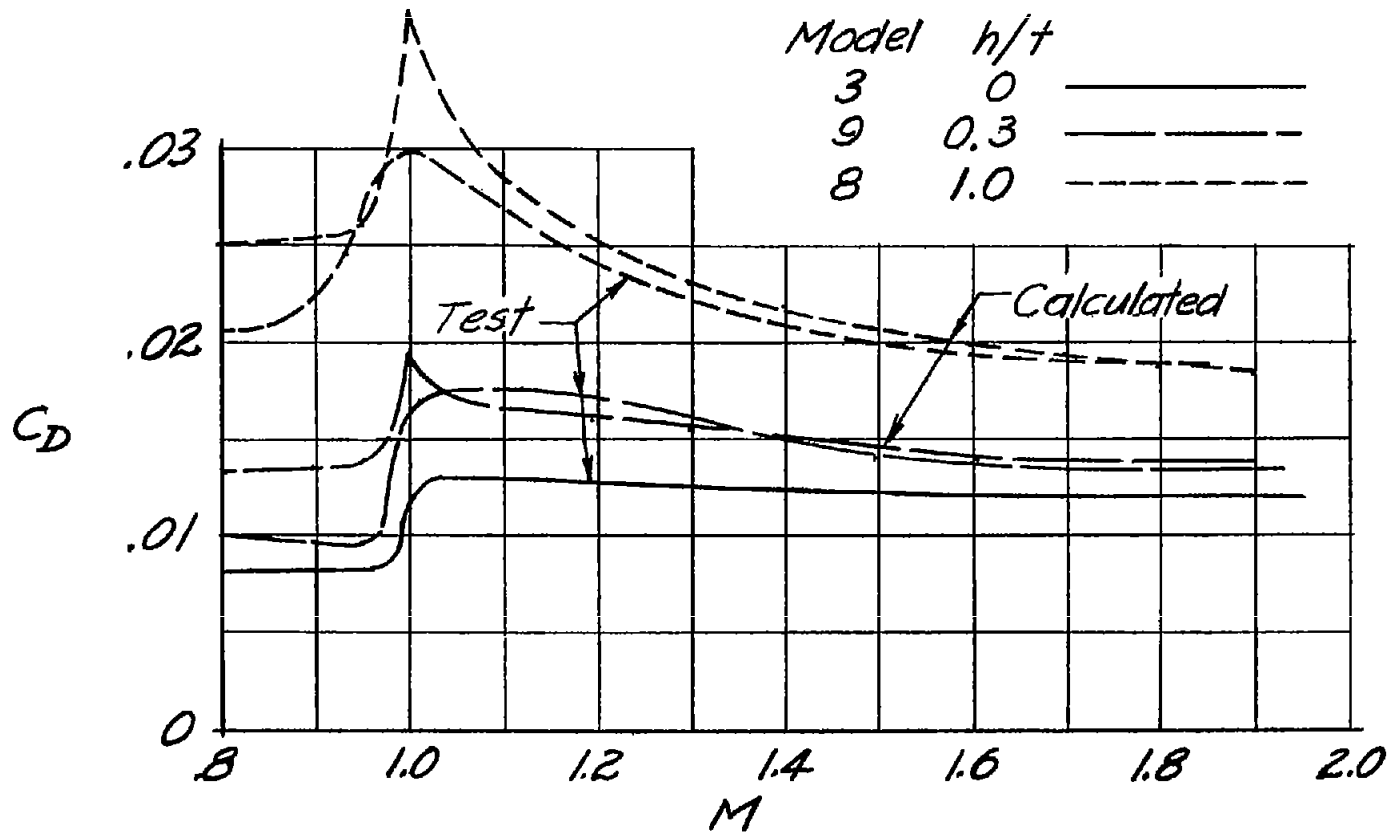


Figure 20.- Effect of trailing-edge thickness.

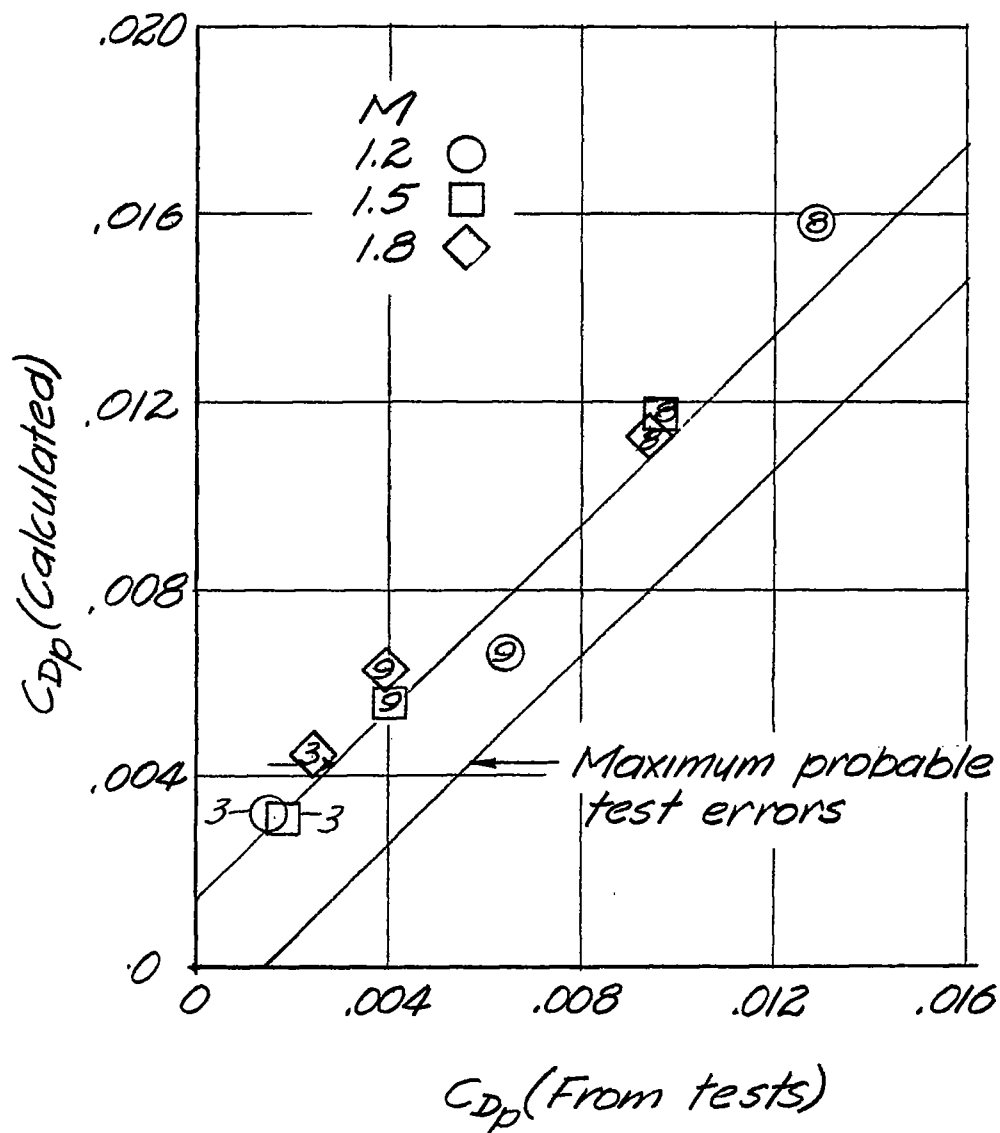


Figure 21.- Comparison of experimentally derived and calculated pressure drag coefficients for series of wings in which trailing-edge thickness is varied. Numbers denote models.



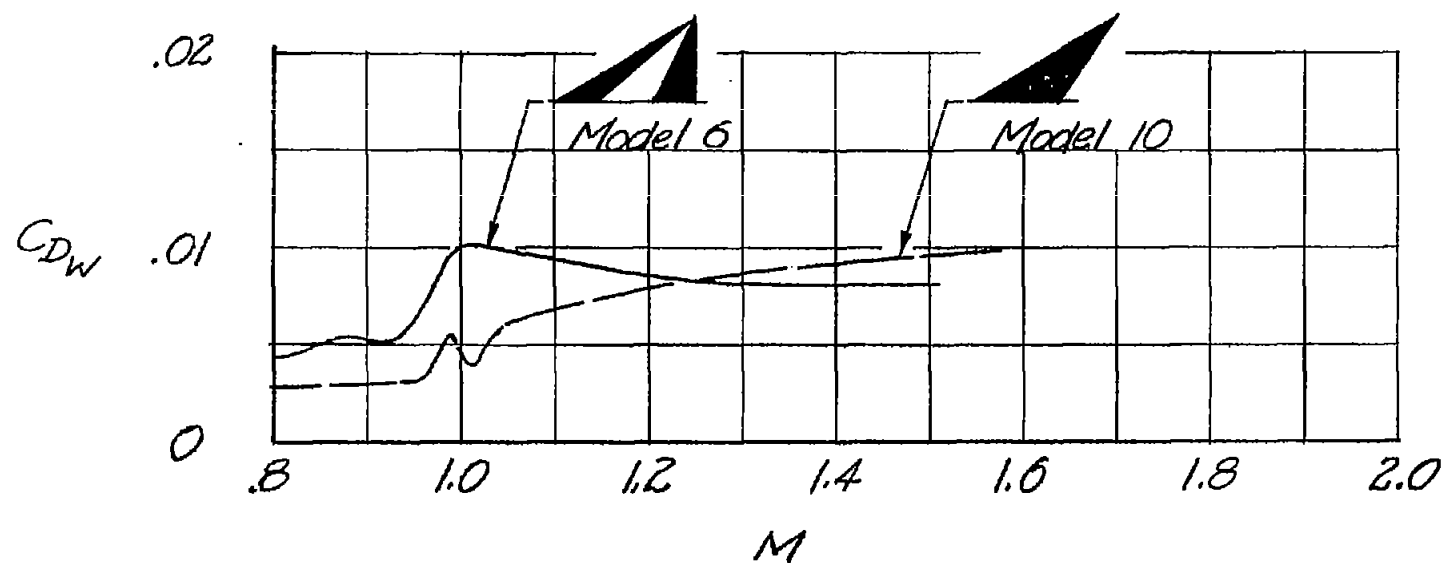


Figure 22.- Effect of shearing afterpart of wing forward. Both wings of same absolute thickness.

Model

11 (present tests)

4 (from ref. 2)

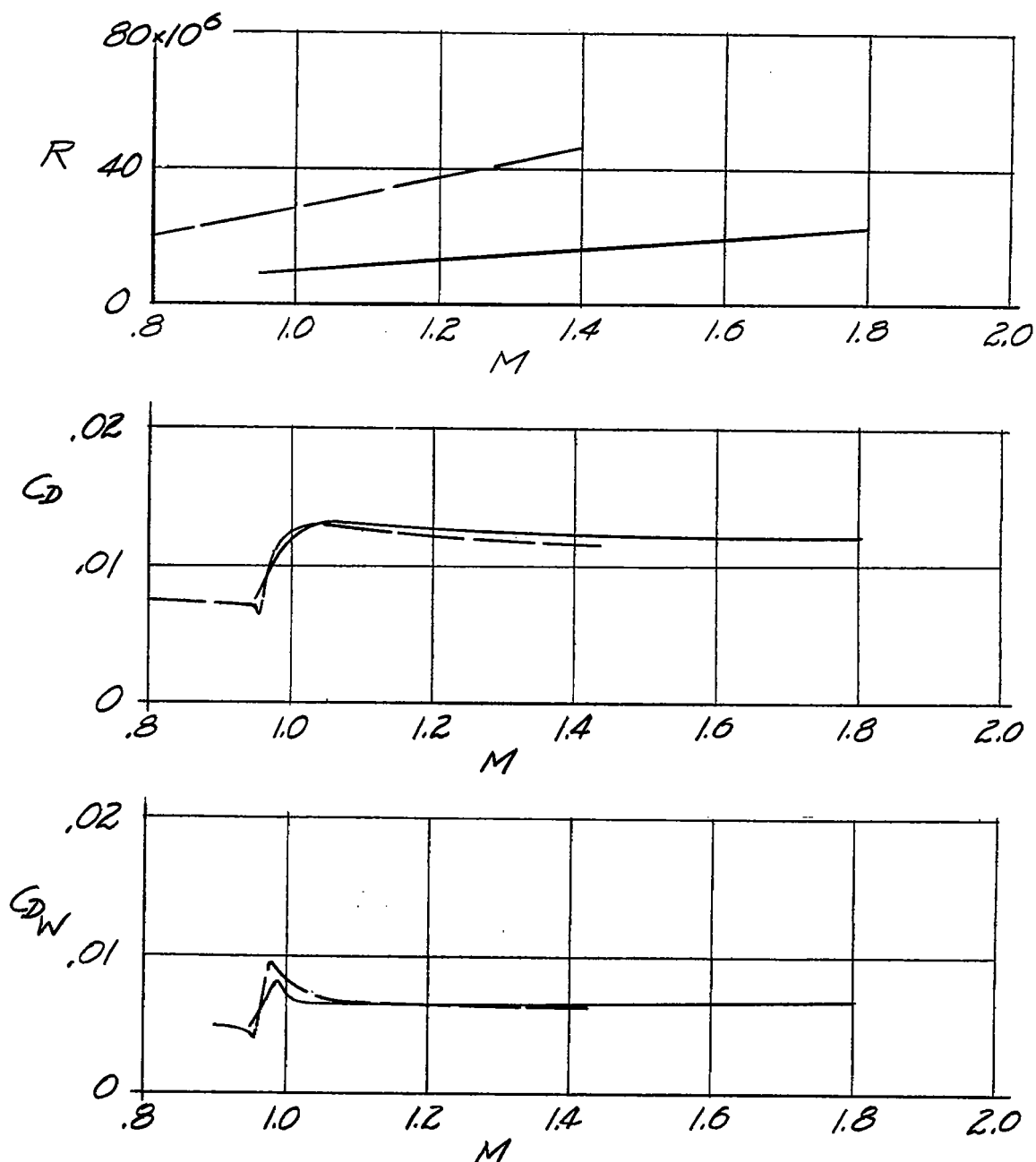


Figure 23.- Effect of model scale on drag.

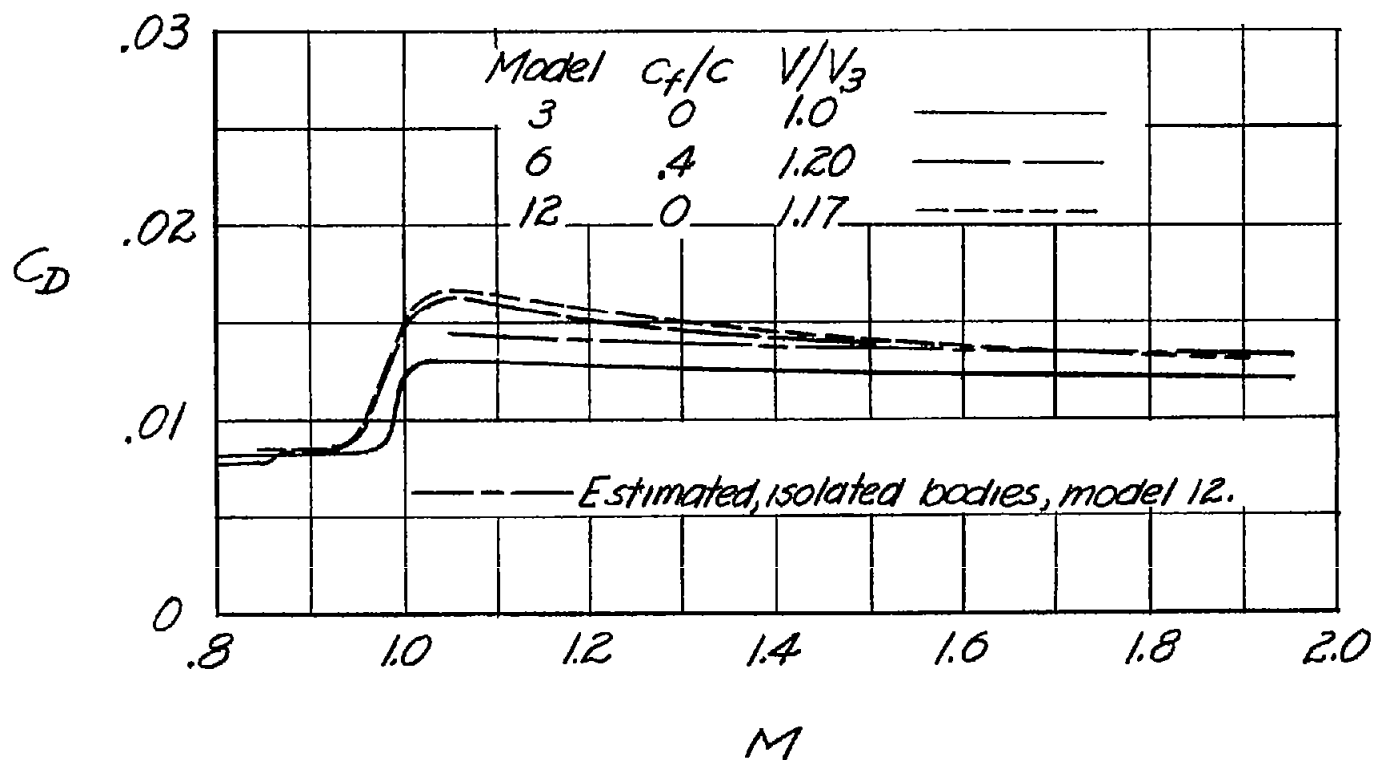


Figure 24.- Effect of simulated control-actuator housings on drag.



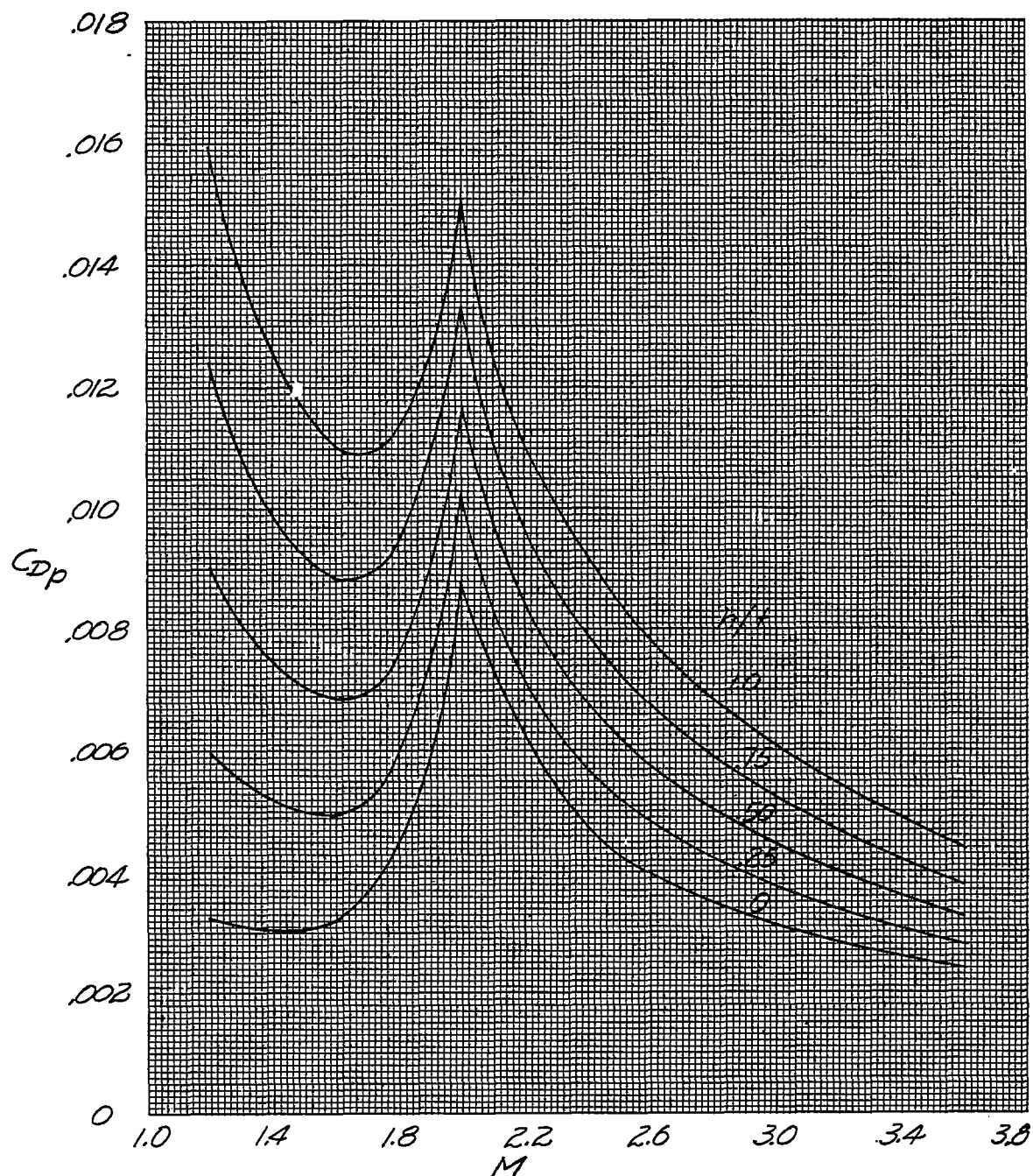


Figure 26.- Calculated pressure drag coefficients for series of wings in which aftersection slopes are varied.  $t/c = 0.03$ .